Effects of Xe ion irradiation on ZrN and the migration behaviour of implanted Eu

by

Thapelo Freddy Mokgadi

Submitted in partial fulfilment of the requirements for the degree of

Magister Scientiae (MSc) in Physics

in the Faculty of Natural and Agricultural Sciences at the University of Pretoria

Supervisor/Promoter: Prof. T.T. Hlatshwayo
Co-Supervisor: Dr. M. Mlambo
Co-Supervisor: Dr. M.J. Madito

December, 2019

DECLARATION OF ORIGINALITY

UNIVERSITY OF PRETORIA

This document must be signed and submitted with every essay, report, project, assignment, dissertation and / or thesis.

Full names of student: **Mr. Thapelo Freddy Mokgadi**

Student number: **10307908**

Declaration

1. I understand what plagiarism is and am aware of the University's policy in this regard.
2. I declare that this **dissertation** is my own original work. Where other people's work has been used (either from a printed source, Internet or any other source), this has been properly acknowledged and referenced in accordance with departmental requirements.
3. I have not used work previously produced by another student or any other person to hand in as my own.
4. I have not allowed, and will not allow, anyone to copy my work with the intention of passing it off as his or her own work.

SIGNATURE OF STUDENT:.....

SIGNATURE OF SUPERVISOR:.....

Dedication

"Whatever your hand finds to do, do it with your might; for there is no work or device or knowledge or wisdom in the grave where you are going."

Ecclesiastes 9 verse 10

This dissertation is dedicated to my loving family; my parents, Mokone and Mmapula Mokgadi, my siblings, Karabo and Ofentse Mokgadi, who have always been my source of confidence, motivation, and support to embark on this journey and face any life challenges with determination, passion and fear of God.

To my late friend and brother Kamohelo Matshoba, until we meet again.

Acknowledgements

I would like to convey my heartfelt appreciation to Prof. T.T. Hlatshwayo, my supervisor, Dr. M. Mlambo and Dr. M.J. Madito, my co-supervisors, for their scientific guidance, support and availability throughout my studies, research and completion of this dissertation.

I am beholden to the students and staff members of the Department of Physics, University of Pretoria, under the leadership of Prof. C.C. Theron, for the wonderful culture that inspires excellence. I want to express my deepest appreciation and thanks to Mr. Z. Abdalla, Mr. M. Ismail, and Mr. H. Abdelbagi, in Prof. T.T. Hlatshwayo and Prof. J.B. Malherbe's group, for providing enormous help in my research.

I am thankful to Dr. E.G. Njoroge for the RBS measurements and insightful suggestions to my research. I am also thankful to Dr. T.T. Thabethe and Mr. T. Ntsoane (NECSA) for the assistance with XRD measurements.

My greatest appreciation goes to my family for their love and support.

Last but not least

Modimo wa matla otlhe, ditebogo tsotlhe di ya go Wena

Summary

Effects of Xe ion irradiation on ZrN and the migration behaviour of implanted Eu

by

Thapelo Freddy Mokgadi

Submitted in partial fulfilment of the requirements for the degree of Magister Scientiae (MSc) in Physics in the Faculty of Natural and Agricultural Sciences at the University of Pretoria

Supervisor/Promoter: Prof. T.T. Hlatshwayo

Co-Supervisor: Dr. M. Mlambo

Co-Supervisor: Dr. M.J. Madito

Owing to its outstanding properties, zirconium nitride (ZrN) has been proposed as a possible candidate for inert matrix for transmutation of long-lived nuclear waste (plutonium and minor actinides) in fast nuclear reactors. In the nuclear reactor environment ZrN will be exposed to different irradiations at elevated temperatures. Under these conditions, it should retain its properties and be able to contain fission products. The irradiation-tolerance of ZrN to slow and swift heavy ions has been investigated and no amorphization was observed. However, little is known about the migration of fission products in ZrN with the exception of He. In this study, the radiation damage retained by swift and slow heavy ions, their annealing and the migration behaviour of implanted europium (Eu) were investigated.

ZrN layers of about 20 μm thick were deposited on silicon substrates using vacuum arc deposition. Some of the deposited ZrN samples were individually implanted with Eu and Xe ions of energy 360 keV all to a fluence of 1.0×10^{16} cm^{-2}, while others were irradiated with 167 MeV

Xe ions to a fluence of 6.77×10^{14} cm^{-2}. Both implantations and irradiation were performed at room temperature. The implanted and irradiated samples were annealed at 800 and 900^{o}C for 5h. The as-deposited samples were characterized by scanning electron microscopy (SEM), grazing incidence x-ray diffraction (GIXRD) and Raman spectroscopy, while implanted and irradiated samples were characterized by Raman spectroscopy and Rutherford backscattering spectrometry (RBS).

GIXRD results confirmed the nano-crystallinity of the deposited ZrN layer. Raman spectroscopy results of the as-deposited ZrN, exhibited all first-order Raman scattering bands indicating a ZrN structure with defects. SHI irradiation produced less concentration of defects compared to the slow energy implantation of Eu and Xe ions. Cubic-Zr_3N_4 phases were observed in swift-heavy ion irradiated ZrN after annealing at 800 and 900^{o}C, while it was not observed in the low energy implanted Xe and Eu samples after annealing at the same temperatures. No migration of implanted Eu was observed after annealing.

Contents

List of Abbreviations

2A Second-order Acoustic mode

2LA Second-order Longitudinal Acoustic mode

2TA Second-order Transverse Acoustic mode

ADS Accelerator-driven Subcritical system

AFCI Advanced Fuel Cycle Initiative

Am Americium

BCC Body centered cubic crystal structure

BZ Brillouin Zone

C Carbon

CRT Cathode Ray Tube

Cs Cesium

CSB cask storage building

Cu Copper

dpa displacement per atom

Eu Europium

FAMA Facility for Modification and Analysis of Materials with Ion Beam

FCC Face centered cubic crystal structure

FLNR Flerov Laboratory on Nuclear Reactions

FR Fast Reactor

FWHM Full-Width-Half-Maxmum

GaN Galium Nitride

Gd Gadolinium

GFR Gas-cooled Fast Reactor

GIF Generation IV International Forum

GIXRD Grazing Incident X-ray Diffraction

HCP Hexagonal Close Packed crystal structure

He Helium

Hf Hafnium

HfN Hafnium Nitride

HTGR High-Temperature Gas-cooled Reactors

I Iodine

ICSD Inorganic Crystal Structure Database

JINR Joint Institute for Nuclear Research

LA Longitudinal Acoustic Mode

LO Longitudinal Optical Mode

LSS Lindhard, Scharff and Schiøtt

LWR Light-Water Reactor

MA Minor Actinide

N Nitrogen

NaCl Sodium Chloride

NECSA Nuclear Energy Corporation

Np Neptunium

Pu Plutonium

PuC Plutonium Carbide

PVD Physical vapour deposition

PyC Pyrolitic Carbon

R path length

RAD Relative atomic density

RBS Rutherford Backscattered Spectrometry

Rn Radon

Rp Projected range

RT Room Temperature

SEM Scanning Electron Microscopy

SHI Swift Heavy ion Irradiation

Si Silicon

SiC Silicon Carbide

Sm Samarium

SFP spent fuel pool

SRIM Stopping and Range of Ions in Matter

TA Transverse Acoustic mode

Te Tellurium

TF Thomas-Fermi

ThC Thorium Carbide

TiN Titanium Nitride

TO Transverse Optical mode

TRISO Tri-Structural Isotropic

TRU-N Transranic Nitride

TWh Terra Watt Hour(s)

U Uranium

UC Uranium Carbide

U-Mo Uranium Molybdenum

UO Uranium Oxide

Xe Xenon

Zr Zirconium

ZrC Zirconium Carbide

ZrN Zirconium Nitride

List of Figures

List of Tables

Chapter 1

Introduction

1.1 Background

Electricity is at the core of the development of any nation. Most of the electricity in the world is generated from burning fossil fuels [1]. This method produces greenhouse gases. The industrialization of the developed world has produced more CO_2 and other greenhouse gases, than we are currently planting trees. The deforestation of the Amazon rainforest has reached a record high in 10 years as recorded by the Brazilian government [2] in 2018. There is so much CO_2 produced as a result of electricity generation from the burning of fossil fuels and the high rising number of cars on our roads. Just recently we have seen the devastating results of climate change due to carbon emissions in Mozambique and Zimbabwe where cyclone Idai wreaked devastation in these two countries [3]. A resounding call has emerged of generating electricity using methods that produce less greenhouse gases. The move away from fossil fuels is an urgent one, the world cannot afford the repercussions of irresponsible use of fossil fuels and the disregard for the environment for mere profit. To mitigate the prevalent emissions, researchers have for years now embarked on investigating alternative energy sources that are as effective as coal and gas, but less damaging to the environment. Different research groups around the world have been established to find solutions and alternatives to the traditional energy generation. One of the contenders for alternative energy sources is nuclear energy. The 2016 global electricity generation breakdown shows that 38.3% was generated from coal and 23.1% from gas, while nuclear energy contributed 10.4% [4]. Coal and gas power stations are cheap to build and Africa has supply of coal and gas, and this is the cheaper option for the

main source of electricity in Africa. However, the long-term cost of the use of coal power stations is always increasing [5]. Globally, the use of electricity from Nuclear energy is growing, its contribution grew from 2477 TWh in 2016 to 2487 TWh in 2017, from about 450 nuclear reactors with 60 more being constructed and amounting to about 15% contribution to the existing capacity [6].

The use of nuclear technology has its own shortcomings. The nuclear power plant incident in Fukushima in 2011 [7], has raised valid questions about nuclear safety. This together with the high initial expense of building a nuclear plant has hindered the progress, interest and buy-in by most countries, especially in the developing world. Nuclear technology also releases high amounts of radioactive waste. In the South African Koeberg nuclear plant, for instance, the spent fuel is stored on-site in what is called a spent fuel pool (SFP) (wet storage) since it is hot and still highly radioactive, figure 1.1 (a). It is then transported to the on-site cask storage building (CSB) (dry storage), figure 1.1 (b). The SFPs storage capacity is reported to be over 90% full and would reach their full capacity by April 2020 [9]. This means that if additional storage space is not created in the SFPs, the plant would have to shutdown prematurely. The problem with dry storage of nuclear waste is that it is not a permanent solution. The spent fuel rods will keep accumulating at the storage site posing possible risks. The Advanced Fuel Cycle Initiative (AFCI) in its goal sees the long term solution to the highly toxic nuclear waste as closing the fuel cycle such that the proliferation of plutonium is not allowed. This would mean that the generated waste will be less toxic. The idea is that the highly toxic and radioactive waste will not have to leave the nuclear plant. The waste would be reconstructed into a new fuel for re-burning [5].

1.2 Motivation

Different fuels such as uranium nitride as well as plutonium nitride in solid solution have been immensely researched for use in nuclear reactors. Uranium has atomic number 92 and nitrogen 7, with uranium having the electron configuration $[Rn]5f^3 6d^2 7s^2$ and nitrogen, $1s^2 2s^2 2p^3$. Because of this, uranium nitride shares similar properties with transuranic nitrides. Transuranics

(a) Wet storage (b) Dry storage

Figure 1.1: *Koeberg's spent fuel storage technology (a) fuel pool and (b) cask storage building [9].*

are elements of the actinide series beyond uranium. Therefore, uranium is at a critical point between the f- and d-orbital dominance. The increase in atomic number in the actinide period stabilizes the f-orbital bringing it's energy closer to the core, while leaving the d-orbital's energy to dominate. The f-orbital and the cubic set mainly dominate in actinium and others, however, generally the chemistry is different from transition metals [10, 11, 12, 13, 14]. The d-orbital is dominant in transuranics, and therefore they share similar traits with transition metals. Transuranics together with their compounds and transition metals also share indistinguishable properties. All transuranic metals are refractory materials exhibiting very high melting points. They are also very brittle and hard as any other cubic nitride. A plethora of data exists on researched actinide carbides such as UC, PuC, (U,Pu)C and ThC, while some data on transuranic carbides is also accessible [15]. These studied carbides have similar structure and physical properties as their nitride forms. The information on these carbides can be used to anticipate the response of the nitrides to similar conditions they have been subjected to. Carbide fuels have been very successful in their use in nuclear research reactors. However, one of the drawbacks of the carbide fuels is their reactivity with water which is a huge hazard for the environment and poses serious reactor safety risks/threats.

Zirconium nitride (ZrN) has been identified as a possible candidate for an inert matrix be-

cause of its excellent chemical and physical properties similar to those of the studied carbides [16]. ZrN is also comparatively a substitute for transuranic nitrides (TRU-N) and also chemically compatible. It has low neutron capture cross-section, high melting point, high thermal conductivity and low vapour pressure [17, 28] which are properties suitable for the reactor environment. Minor actinides (MA: Np, Am, Cm) are perfectly soluble in ZrN. Because of this, plutonium can be directly burnt-up and the long-lived actinides transmuted in the fast nuclear reactors (FR) or accelerator-driven subcritical system (ADS) [19, 20, 21]. ZrN can also be used as a fuel phase in generation IV Gas-cooled Fast nuclear Reactor (GFR) [19, 22].

1.3 Previous work

In a nuclear reactor environment, ZrN will be exposed to different irradiations from the fission products at extreme temperatures. Therefore, the behaviour of this material under these conditons is vital. The irradiation tolerance of ZrN has been investigated (Egeland et al., 2013) [23]. Xenon and Krypton heavy ions were implanted into ZrN at energy 300 keV up to a displacement damage of 200 dpa. No evidence of any amorphization was observed from GIXRD results.

Helium, Xenon and in some cases Bismuth of energies 30 keV, 167 MeV and 695 MeV, respectively, were implanted in ZrN samples and were subsequently annealed between 600 and 1000^oC for 20 minutes by (van Vuuren et al., 2015) [24]. Annealing was found to cause peeling at a depth consistent with the end-of-range of 30 keV He ions. However, irradiation with swift heavy ions was found to stifle the formation of blisters.

Xenon ions of energy 167 MeV at fluences in the range $3\times10^{12}-2.6\times10^{15}cm^{-2}$, 250 MeV Krypton at fluences $1\times10^{13}-7.06\times10^{13}\,cm^{-2}$ and 695 MeV Bismuth at fluences $10^{12}-10^{13}\,cm^{-2}$ were implanted on nano-structured ZrN layers of $0.1, 3, 10$, and $20\,\mu m$ thickness. (van Vurren et al., 2013) [25] found that the nanocrystallinity of ZrN was not affected by irradiation for the $0.1\,\mu m$ thick layer even at high fluences. Therefore, the nanocrystalline layers were found to be very resistant to radiation damage due to SHIs.

Nanocrystalline ZrN was implanted with 800 keV Argon ions to study the radiation effect on ZrN. After irradiation at $10^{14}\ cm^{-2}$, (Craciun et al., 2015) [17] found that there was an insignificant change in crystallite size. However, a dose of $10^{15}\ cm^{-2}$ resulted in decrease in crystallite size followed by a decline in nanohardness and Young modulus.

2.6 MeV of Protons at 800^oC were implanted by (Yang et al., 2009) [26] to study the radiation stability of ZrN. Irradiation doses of 0.35 and 0.75 dpa resulted in an excess of nano-sized defects with some identified as vacancy-type pyramidal dislocation loops. However, the irradiated samples did not result in any voids or bubbles, and no amorphization was observed.

The radiation tolerance of nanocrystalline ZrN irradiated with 900 keV Iron(II) ions at a 40^o incident angle to a fluence of 6×10^{15} cm^{-2} up to a dose of 10 dpa was investigated by (Jiao et al., 2015) [27]. Films with the grain size of about 9 nm exhibited less radiation damage corroborated by a low lattice parameter, less radiation softening and less resistivity. The bigger grain sized sample resulted in notable radiation softening credited to the increase in radiation defects in the grains.

In all the previous irradiation tolerance studies above, ZrN indicated high radiation tolerance with no amorphization and in the case of He is implanted ZrN, irradiating with swift heavy ions suppresses the formation of blisters. However, few studies have been made on the migration and diffusion behaviour of implanted fission products apart from He in ZrN [25]. This study investigated the effects of swift heavy Xe ions of 167 MeV at a fluence of $6.77 \times 10^{14}\ cm^{-2}$ and slow Xe and Eu ions of energy 360 keV at a fluence of $1.0 \times 10^{16}\ cm^{-2}$. The ion irradiated ZrN deposited onto Si substrates was characterized by Raman spectroscopy, grazing incidence X-ray diffraction (GIXRD) and Rutherford backscattered spectrometry (RBS).

1.4 Dissertation outline

The rest of this dissertation is organized as follows: chapter 2 discusses ZrN, its synthesis, structure and fabrication. Chapter 3 discusses the different types of nuclear reactors. Chapter

4 presents the irradiation theory. Chapter 5 discusses the different experimental techniques used in this study. Chapter 6 presents the experimental methods. Chapter 7 provides Results and discussion while chapter 8 Summarizes the findings and future work. The Appendix is in the last section.

Bibliography

[1] Mpoweruk.com, (2020). *Electrical Power Generation from fossil fuels.* [Online] Available at: https://mpoweruk.com/fossil_fuels.htm [Accessed 19 Jan. 2020]

[2] Ministério do Meio Ambiente, (2018). 'Taxa de desmatamento na Amazônia Legal ', viewed 27 May 2019. http://www.mma.gov.br/informma/item/15259-governo-federal-divulga-taxa-de-desmatamento-na-amaz\%C3\%B4nia.html

[3] Unicef.org, (2020). *Cyclone Idai and Kenneth.* [Online] Available at: https://www.unicef.org/mozambique/en/cyclone-idai-and-kenneth [Accessed 19 Jan. 2020]

[4] International Energy Agency, (2018). 'Key world energy statistics', 2, 14, viewed 27 May 2019. https://webstore.iea.org/download/direct/2291?fileName=Key_World_2018.pdf

[5] Egeland, G. W., (2005). 'Radiation damage and fission product release in zirconium nitride'. Doctor of Philosophy Thesis, New Mexico Institute of Mining and Technology, Socorro, New Mexico.

[6] Ho, M., Obbard, E., Burr, P. A., and Yeoh, G., (2019). 'A review on the development of nuclear power reactors'. *Energy Procedia.* Vol. 160, pp. 459-466

[7] Lipscy, P.Y., Kushida, K.E., and Incerti, T., (2013). 'The Fukushima disaster and Japan's nuclear plant vulnerability in comparative perspective'. *Environmental science & technology*, 47(12), p6082-6088

[8] Compton, K.T., (1946). 'If the atomic bomb had not been used'. *The Atlantic Monthly.*

[9] Roelf, W., (2020). *Waste storage at Koeberg nuclear plant brimming — IOL Business Report.* [onlin]Iol.co.za. Available at: https://www.iol.co.za/business-report/

energy/waste-storage-at-koeberg-nuclear-plant-brimming-37936997 [Accessed 21 Jan. 2020]

[10] Scott, P., Kalstsoyannis, N., (1999). 'The f element'. *Oxford Chemistry Primers, Oxford Science Publication*, no. 76

[11] Takano, M., Itoh, A., Akabori, M., and Ogawa, T., (2001). 'Oxygen Solubility in dysprosium mononitride prepared by carbothermic synthesis'. *Journal of Alloys and Compounds*, 327(1-2), pp. 235-239

[12] Takano, M., Itoh, A., Akabori, M., Ogawa, T., Namata, M., and Okamoto, H., (2001). 'Carbothermic synthesis of (Cm,Pu)N'. *Journal of Nuclear Materials*, 294(1-2), pp. 24-27

[13] Ogorodnikov, V.V., and Rogovoi, Y.J., (1993). 'Regularities in the Changes of Properties of Cubic, Transition Metal Mononitrides'. *Inorganic Materials*, 29(4), pp. 591

[14] Ogawa, T., (1994). 'Structural stability and thermodynamic properties of Zr-N alloys'. *Journal of Alloys and Compounds*, 203(1-2), pp. 221-227

[15] Matzke, Hj., (1986). *Science of advanced LMFBR fuels*, 1st edn, North Holland, Amsterdam

[16] Wu, D.,Zhang, Z., Fu, D., Fan, W. and Guo, H., (1997). 'Structure, electrical and chemical properties of zirconium nitride films deposited by dc reactive magnetron sputtering'. *Applied Physics A: Materials Science & Processing*, 64(6)

[17] Craciun, D., Socol, G., Dorcioman, G., Simeone, D., Gosset, D., Behdad, S., Boesl, B. and Craciun, V., (2015). 'Ar ions irradiation effects in ZrN thin films grown by pulsed laser deposition'. *Applied Surface Science*, 336, pp.129-132.

[18] Adachi, J., Kurosaki, K., Uno, M., and Yamanaka, S., (2005). 'Thermal and electrical properties of zirconium nitride'. *Journal of alloys and compounds*, 399(1-2), pp.242-244

[19] Bao, W., Robertson, S., Liu, J. X., Zhang, G. J., Xu, F., and Wu, H. (2018). 'Structural integrity and characteristics at lattice and nanometre levels of ZrN polycrystalline irradiated by 4 MeV Au ions'. *Journal of the European Ceramic Society*, 38(13), pp. 4373-4383.

[20] Wheeler, K., Peralta, P., Parra, M., McClellan, K., Dunwoody, J., and Egeland, G. (2007). 'Effect of sintering conditions on the microstructure and mechanical properties of ZrN as a surrogate for actinide nitride fuels'. *Journal of Nuclear Materials*, 366(3), pp. 306-316.

[21] Tang, Y., Zhang, G. J., Xue, J. X., Wang, X. G., Xu, C. M., and Huang, X. (2013). 'Densification and mechanical properties of hot-pressed ZrN ceramics doped with Zr or Ti'. *Journal of the European Ceramic Society*, 33(7), pp. 1363-1371.

[22] Meyer, M. K., Fielding, R., and Gan, J. (2007). 'Fuel development for gas-cooled fast reactors'. *Journal of Nuclear Materials*, 371(1/3), pp. 281-287.

[23] Egeland, G.W., Valdez, J.A., Maloy, S.A., McClellan, K.J., Sickafus, K.E. and Bond, G.M., (2013). 'Heavy-ion irradiation defect accumulation in ZrN characterized by TEM, GIXRD, nanoindentation, and helium desorption'. *Journal of nuclear materials*, 435(1-3), pp.77-87.

[24] van Vuuren, A.J., Skuratov, V., Uglov, V. and Sohatsky, A., (2015). 'Swift heavy ion irradiation effects on He agglomeration in ZrN and TiZrN ceramics'. *The interaction of radiation with a solid*, 156, pp. 91–92.

[25] van Vuuren, A.J., Skuratov, V.A., Uglov, V.V., Neethling, J.H. and Zlotski, S.V., (2013). 'Radiation tolerance of nanostructured ZrN coatings against swift heavy ion irradiation'. *Journal of Nuclear Materials*, 442(1-3), pp.507-511.

[26] Yang, Y., Dickerson, C. A., and Allen, T. R. (2009). 'Radiation stability of ZrN under 2.6 MeV proton irradiation'. *Journal of Nuclear Materials*, 392(2), pp. 200-205.

[27] Jiao, L., Yu, K.Y., Chen, D., Jacob, C., Shao, L., Zhang, X. and Wang, H., (2015). 'Radiation tolerant nanocrystalline ZrN films under high dose heavy-ion irradiation'. *Journal of Applied Physics*, 117(14), p.145901

Chapter 2

Zirconium Nitride

Zirconium nitride is resistant to heat and hard to melt, due to its interesting combination of ionic, covalent and metallic bonding. Its melting point is approximately 2980 ^{o}C. It has good electrical and thermal conductivities and good superconducting abilities. Its good corrosion resistance property makes it a perfect coating material for structural materials and cryogenic thermometers. It has low neutron capture cross-section making it suitable for nuclear environments. When coating in high wear and corrosive environments, it is applied using the physical vapour deposition (PVD) coating process. However, ZrN reacts too rapidly with oxygen even at temperatures below 600 ^{o}C [1, 2]. Hence, the deposition of ZrN should be done in a controlled environment, to evade oxidation [3]. The gold luster polish gives zirconium nitride a metallic shine which is good for very abrasion-resistant decorative coatings. This chapter discusses the synthesis of ZrN, its crystal structure, and physical properties.

2.1 Synthesis

Zirconium nitride can be produced using various processes and techniques. It can be synthesized using chemical vapour deposition for tribological and cosmetic coatings for instance [4]. In cases where brittle and thermally sensitive substrates are used in the processing and fabrication of semiconductor components, physical vapour deposition (PVD) techniques are used [5]. These PVD techniques involve sputter deposition [6], reactive ion platting, and arc deposition or evaporation techniques [8]. Carbothermal reduction-nitridation is used for synthesis

of ZrN powders [1]. Chemical composition, long-range crystalline structure and the amount and nature of impurities can be tuned to influence the material's properties for a specific function. In this project ZrN layers were deposited by arc deposition. Fabrication of the layers was done utilizing a balance of cathodic arc and magnetron deposition [9]. The former is a physical vapour deposition technique in which an electric arc is utilized to vaporize material from a cathode target, and the latter is a plasma deposition technique where the positively charged particles from the plasma are accelerated from the target towards the substrate, and the unbalanced magnetic field is utilized to trap quick moving secondary ions that escape from the target surface.

2.2 Crystal Structure and Phases

Zirconium nitride with stoichiometry (1:1) is its most stable form. At the Zr/N ratio ≥ 1.33, Zr_3N_4 phase is formed; this phase is grey and displays insulating properties [10]. Rock-salt is the structure of stoichiometric ZrN, where both zirconium and nitrogen atoms form isolated FCC lattices. In the octahedral interstices of the FCC zirconium lattice lies the nitrogen atoms and furthermore nitrogen forming an FCC sublattice. Literature puts the lattice parameter for ZrN at around 4.577 $\AA$ with density 7.09 g/cm^3 [4, 6]. If the corner of the ZrN lattice is at $0, 0, 0$ position, the N position is at position $\frac{1}{2}, \frac{1}{2}, \frac{1}{2}$ as shown in figure 2.1. The Zr_3N_4 phase is firmly identified with the B1 (NaCl) structure of the mononitrides, yet it demonstrates a little rhombohedral distortion.

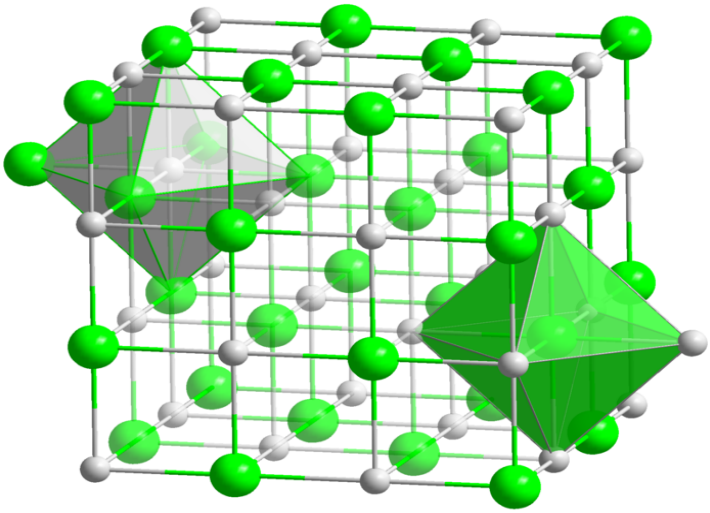

Figure 2.1: *Crystal structure of stoichiometric ZrN (Zr-green, N-white) [13].*

.

At room temperature, Zr metal has an hcp structure with an α phase which does not dissolve nitrogen easily. There are at least three crystal structures between the Zr metal and the stoichiometric ZrN. The β (bcc) phase for the metal Zr forms at 863 ^0C and contributes to dissolving nitrogen atoms into the metal although it exists at higher temperatures. As the nitrogen atoms are dissolved into the metal β-Zr (in figure 2.2), the structure is rearranged back into an α (hcp) phase with nitrogen dissolved in this structure [15]. ZrN at higher temperatures rearranges itself from bcc to hcp and then to fcc with increasing nitrogen thereby increasing symmetry up to the perfect Zr/N stoichiometry. This follows the nitrogen's s and p orbital contributions to the transition metal's d-orbital and therefore reducing the energy by changing the symmetry [16]. The α phase begins to change into a cubic phase at about 21 atomic percent nitrogen, until it is complete at about 45 atomic percent nitrogen. This resulting cubic structure is the NaCl structure with nitrogen deficient sub-lattice. Nitrogen atoms can readily occupy the sub-lattice, however it is not simple to reach a perfect 1:1 ratio of Zr/N in ZrN and other cubic nitrides [17]. A familiar phenomenon in cubic carbides and nitrides is the habit of nitrogen vacancies creating short-range ordered superstructures close to the α-cubic transformation line [18, 19]. This cubic structure has been postulated to be a stacked set of NaCl unit cells with an ordered array of nitrogen vacancies.

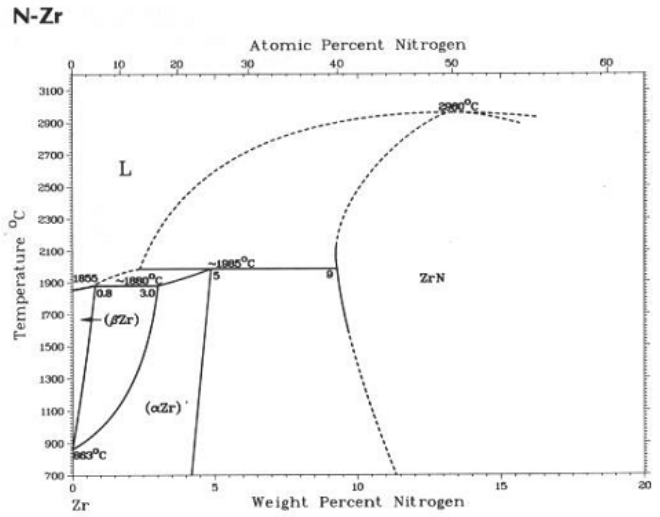

Figure 2.2: *Zr-N binary phase equilibrium diagram [14].*

2.3 Physical Properties

Table 2.1 shows the physical properties of ZrN. Zirconium nitride's crystal structure and relatively strong covalent bonding gives it its hardness and high elastic modulus. These properties are closely related to the defects in the material. The large stalking fault energy is as a result of the strong covalent bonding. It has been adopted that the zirconium metal has a displacement threshold energy averaged over all lattice directions (E_d) of $40 \pm 8\,eV$, and an effective threshold energy (E_{deff}) used in the analyses of irradiation in reactors of $57 \pm 11\,eV$ [20]. However the displacement threshold energy of ZrN is not directly reported on. Therefore a reasonable E_d range can be estimated from contrasting with similar ceramics such as GaN and 3C-SiC. The averaged displacement energy of Ga is $73,2\,eV$ in GaN and N is $32,4\,eV$ while the minimum E_d is $39\,eV$ and $17\,eV$, respectively, both along the direction $< \bar{1}010 >$ [21]. C and Si's minimum displacement energies were found to be $20\,eV$ and $49\,eV$, respectively, along the direction $< 100 >$ in 3C-SiC [22]. The average displacement energy for Zr and N in ref [23] were chosen to be $35\,eV$ and $25\,eV$, respectively, based on the estimation from ZrC, and since N and C are close to each other.

Table 2.1: Physical Properties of ZrN [6, 11]

Structure	NaCl, B1, fm3m
Lattice Parameter	4.5675 $\mathring{A}$
Density (300K)	7.09 g/cm^3
Hardness	$\sim$ 20 GPa
Young's Modulus	$\sim$ 460 GPa
Heat Capacity (300K)	$\sim$ 41 $kJ/mol.K$
Thermal Conductivity (300K)	400 $W/m.K$
Melting Temperature	2980 ^0C

Bibliography

[1] Pilloud, D,, Pierson, J.F., Cavaleiro, A., Marco de Lucas, M.C., (2005). 'Effect of germanium addition on the properties of reactively sputtered ZrN films'. *Thin solid films*, 498 (1-2), pp. 180-186.

[2] Del Re, M., Gouttebaron, R., Dauchot J.P., Hecq, M., (2004). 'Study of the optical properties of AlN/ZrN/AlN low-e coating'. *Surface and coatings technology*, 180-181, pp. 488-495

[3] Panjan, P., Ẑabkar, A., Navinŝek, B., Demŝar, A., Ŝvajger, A., Tanović , L., Tanović , N., (1990). 'Optical properties of nitride coatings deposited at low substrate temperatures'. *Vacuum*, 40(1-2), pp. 161-163

[4] Wendel, H. and Suhr, H., (1992). 'Thin zirconium nitride films prepared by plasma-enhanced CVD'. *Applied Physics A*, 54(4), pp.389-392.

[5] Fillit, R.Y., Perry, A.J. and Strandberg, C., (1991). 'X-ray elastic constants, stress profiling and composition of physically vapor deposited ZrN films'. *Thin Solid Films*, 197(1-2), pp.47-55.

[6] Sell, J.A., Meng, W.J. and Perry, T.A., (1992). 'Diagnostics of dual source reactive magnetron sputter deposition of aluminum nitride and zirconium nitride thin films'. *Journal of Vacuum Science & Technology A: Vacuum, Surfaces, and Films*, 10(4), pp.1804-1808.

[7] Yin, L., Xu, Y., Huang, Z., Liu, Y.G., Fang, M., and Liu, B., (2013). 'Synthesis of ZrN-Si3N4 composite powders from zircon and quartz by carbothermal reduction and nitridation'. *Powder technology*, 246, pp. 677-681.

[8] Johnson, P.C. and Randhawa, H., (1987). 'Zirconium nitride films prepared by cathodic arc plasma deposition process'. *Surface and Coatings Technology*, 33, pp.53-62.

[9] Constable, C.P., Yarwood, J. and Mü nz, W.D., 1999. Raman microscopic studies of PVD hard coatings. Surface and Coatings Technology, 116, pp.155-159.

[10] Micelotta, E. R., Jones, A. P., Tielens, A. G. G. M., (2010). 'Polycyclic aromatic hydrocarbon processing in interstellar shocks'. *Astronomy and Astrophysics, A36*, 510

[11] PCPDFWIN, P.D.F., (2000). Version 2.1 JCPDS. *The international Centre for Diffraction Data*

[12] Lanjani, M.M., Kiani, M., Tanhayi, M. and Majdabadi, A., (2011). 'Characterization of ion beam sputtered ZrN coatings prepared at different substrate temperatures'. *Crystal Research and Technology*, 46(4), pp. 351-356

[13] `https://upload.wikimedia.org/wikipedia/commons/c/c0/NaCl_polyhedra.png` Accessed 13 July 2019

[14] Gras, J.M., (2014). 'State of the art of 14C in Zircaloy and Zr alloys-14C release from zirconium alloy hulls (D3. 1)'. CAST Project Report.

[15] Domagala, R.F., McPherson, D.J. and Hansen, M., (1956). 'System zirconium-nitrogen'. *JOM*, 8(2), pp.98-105.

[16] Brewer, L., (1968). 'Bonding and structures of transition metals'. *Science*, 161(3837), pp.115-122.

[17] Toth, L.E., (1971). 'Refractory Materials, Transition Metal Carbides and Nitrides'. Academic Press Inc., New York, 7, p.88.

[18] Li, P. and Howe, J.M., (2003). 'Short-range ordering and 1, 1/2, 0 diffuse intensity maxima in ZrN_x'. *Acta materialia*, 51(5), pp.1261-1270.

[19] Sauvage, M.T. and Parthe, E., (1972). 'Vacancy short-range order in substoichiometric transition metal carbides and nitrides with the NaCl structure. II. Numerical calculation of vacancy arrangement'. *Acta Crystallographica Section A: Crystal Physics, Diffraction, Theoretical and General Crystallography*, 28(6), pp.607-616.

[20] Konobeyev, A.Y., Fischer, U., Korovin, Y.A. and Simakov, S.P., (2017). 'Evaluation of effective threshold displacement energies and other data required for the calculation

of advanced atomic displacement cross-sections'. *Nuclear Energy and Technology*, 3(3), pp.169-175.

[21] Jiao, L., Yu, K.Y., Chen, D., Jacob, C., Shao, L., Zhang, X. and Wang, H., (2015). 'Radiation tolerant nanocrystalline ZrN films under high dose heavy-ion irradiations'. *Journal of Applied Physics*, 117(14), p.145901.

[22] Gao, F., Xiao, H.Y. and Weber, W.J., (2011). 'Ab initio molecular dynamics simulations of low energy recoil events in ceramics'. *Nuclear Instruments and Methods in Physics Research Section B: Beam Interactions with Materials and Atoms*, 269(14), pp.1693-1697.

[23] Yang, Y., Dickerson, C.A. and Allen, T.R., (2009). 'Radiation stability of ZrN under 2.6 MeV proton irradiation'. *Journal of Nuclear Materials*, 392(2), pp.200-205.

[24] van Vuuren, A.J., (2014). *Swift Heavy Ion Radiation Damage in Nanocrystalline ZrN* (Doctoral dissertation, Nelson Mandela Metropolitan University)

Chapter 3

Nuclear Reactors

Nuclear reactors are the source of nuclear power for electricity generation. The nuclear energy needed to generate electricity is extracted from nuclear fission reactions. Fission reactions occur inside a nuclear core in a nuclear fuel, where uranium and other fissile materials undergo a nuclear chain reaction propagated by thermal or fast neutrons. Fast or high energy neutrons are easily absorbed by fissile materials which then fission and produce energy. The energy from fission is then used for electricity generation.

There are mainly two types of nuclear reactors. The thermal and the fast (also called breeders) nuclear reactors, which are based on the neutron energy spectrum. Thermal reactors uses slow or thermal neutrons and a moderator to slow down the neutrons. The fast neutron reactors use fast neutrons which are in the energy region of 5 MeV or greater and do not use any moderator. This chapter discusses the two types of nuclear reactors, that is thermal reactors and fast reactors, it also discusses the advanced reactors and the generation IV initiatives.

3.1 Thermal Reactors

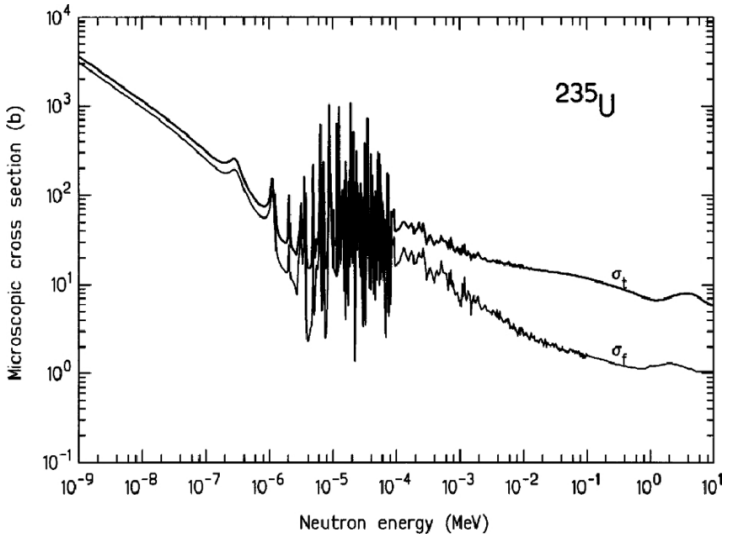

Figure 3.1: *Total and fission cross-section of* ^{235}U *[1].*

Fission reactions in nuclear reactors produce various sizes of fission products, with each step producing three highly energetic neutrons [2]. The reaction cross-section of a neutron in a reactor is indirectly proportional to its energy, that is, the reaction cross-section increases with a decrease in neutron energy. The thermal neutron's reaction cross-section depends heavily on the fissile material it interacts with. Therefore, how much the reaction cross-section increases is dependent on the fissile material. Figure 3.1 shows the cross-section of ^{235}U nuclear fission. Nuclear fission reactions produce high energy/thermal neutrons in the thermal reactor. Therefore, in order to moderate these neutrons a material is used called a moderator. A moderator is a material with low neutron capture cross-section, and it helps increase the reaction cross-section and neutron-atom interaction by lowering the energetic neutrons. In showing the performance of a moderator, the moderating power and moderating ratio are essential, and they are given by [2]

$$moderating\,power = \xi\Sigma_s \tag{3.1}$$

$$moderating\,ratio = \xi \frac{\Sigma_s}{\Sigma_a} \tag{3.2}$$

where ξ is the logarithmic energy decrement, which is the rate of energy loss by elastic scattering, and Σ_s is the macroscopic cross-section of scattering while Σ_a is that of absorption. For typical moderators, the values are given in Table **??**, where α is the maximum rate of energy loss due to the collision with the nucleus of atomic number A. ^{238}U is not a moderator but is given as a reference for comparison.

^{238}U is not fissile and contributes about 99.27% of naturally occurring uranium's mass while the rest is the fissile ^{235}U and some trace amounts of ^{234}U [3]. Using this as a fuel will cause most of the neutrons to be absorbed by ^{238}U, as can be seen in figure 3.2. ^{238}U has very high neutron absorption called resonance absorption at an energy slightly less than 10 eV as compared to the low absorption of ^{235}U in figure 3.1. Resonance absorption is associated with the nucleus energy levels in an atom. It is a region where the cross-section rapidly changes from about one to 10^5 barns in a small fraction of energy of about $1\,eV$ [2]. Therefore, natural uranium as a fuel will only lead to ^{238}U absorbing most of the neutrons and this will make it hard for the nuclear reactor to reach criticality. Hence, the solution to this is to enrich ^{235}U, albeit at a high cost of enrichment. The other option is to allow for a heterogeneous arrangement, that is the separation of fuel and moderator in the nuclear reactor. Both diffusion and moderation occur inside the moderator, while inside the fuel only diffusion of neutrons is dominant since the fuel is heavy to moderate neutrons. Therefore, having the nuclear reactor in a heterogeneous arrangement means the neutrons scattered in the fuel will likely have consecutive collisions inside the fuel, while those scattered in the moderator will thus likely have consecutive collisions in the moderator. This is important because that means the neutrons produced as a result of the fission reactions inside the fuel will not be moderated in the fuel, rather they will escape the fuel into the moderator and will slowly lose their energy. These neutrons will diffuse back into the fuel once they reach a particular low energy. When the neutron energies reach the resonance absorption region the diffusion into the fuel is blocked and the neutrons are absorbed on the surface of the fuel in an act of self-shielding [2]. The diffusion process will continue until finally the neutrons are moderated to thermal neutrons in the moderator and ultimately be absorbed by ^{235}U. As for the resonance absorption in

Table 3.1: Characteristics of typical moderators [2]

Moderator	A	α	ξ	Density (g/cm^3)	No. of collisions, 1 eV to 2 MeV	$\xi\Sigma_s\,(cm^{-1})$	$\xi\frac{\Sigma_s}{\Sigma_a}$
H	1	0	1	gas	14	-	-
D	2	0.111	0.725	gas	20	-	-
H_2O	-	-	0.920	1.0	16	1.35	71
D_2O	-	-	0.509	1.1	29	0.176	5670
He	4	0.360	0.425	gas	43	1.6×10^{-5}	83
Be	9	0.640	0.209	1.85	69	0.158	143
C	12	0.716	0.158	1.60	91	0.060	192
^{238}U	238	0.983	0.008	19.1	1730	0.003	0.0092

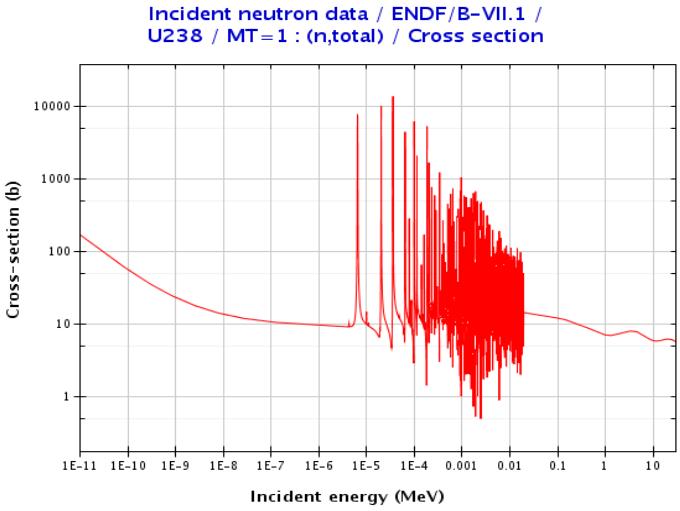

Figure 3.2: *Fission cross-section of* ^{238}U*. [4].*

the reactor, it can be substantially minimized by increasing the amount of self-shielding. This can be done by creating a bigger fuel rod to reduce the ratio of the fuel surface area and volume. The widely operated thermal nuclear reactor today is the light-water reactor and it uses enriched uranium and has the heterogeneous arrangement adopted in it's design [2].

3.2 Fast Reactors

The high energy of neutrons in the reactor causes increase in the fission cross-section, but this also increases the capture cross-section, which is a big problem for thermal reactors because of the moderator. The number of neutrons emitted η, as a result of the absorption by a fissile material can be calculated as [2]:

$$\eta = \nu \frac{\sigma_f}{\sigma_f + \sigma_c} \tag{3.3}$$

where σ_f is the fission cross-section, σ_c capture cross-section and ν the mean number of emitted neutrons per nuclear fission. Figure 3.3 shows the relationship between η and the dependence on the energy of the colliding neutrons. The number of neutrons released per neutron absorbed, η is about 2 for thermal neutrons, but from about 0.1 MeV energy the number of neutrons released increases swiftly. This could produce enough neutrons to maintain a chain reaction and generate surplus neutrons. If these surplus neutrons could be absorbed by ^{238}U, ^{239}Pu would be generated, thereby burning fissile materials while generating fissile products. The conversion ratio is the number of produced fissile products per the number of burned fissile atoms. Therefore a conversion ratio of over one can be achieved if the η-value is adequately above 2, making it possible to produce (breed) more fissile material than burned. The type of reactor that can do this is called a breeder/fast nuclear reactor because it uses fast (high energy) neutrons to breed new fissile material. ^{233}U in figure 3.3 in the thermal region has a slightly high η-value than 2, meaning that breeding is achievable with thermal neutrons.

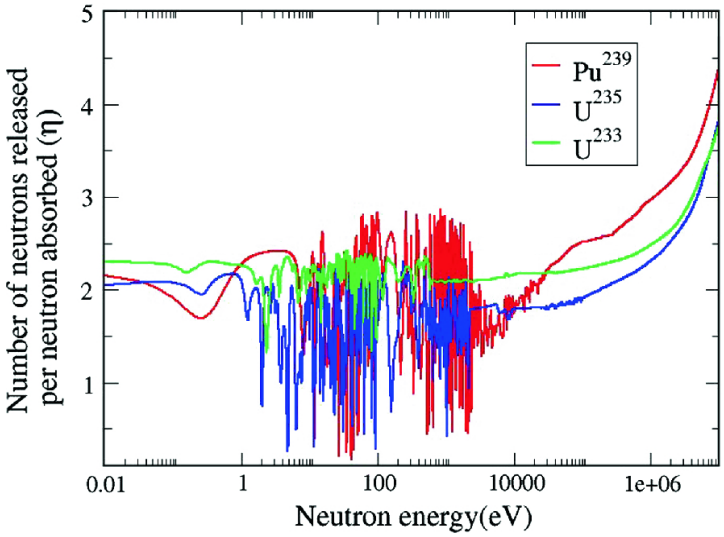

Figure 3.3: *Number of neutrons released per neutrons absorbed (η-values) for ^{233}U, ^{235}U, and ^{239}Pu [5].*

3.3 Advanced Reactors and Gen IV Initiative

There are broadly two types of nuclear reactors which were covered above, but there exists many configurations of these reactors. Some of them are used as test reactors to test the practicality of advanced designs while others are designed to generate transuranics for study.

Generation IV International Forum (GIF) is an international attempt to set up research and development to institute the practicality and performance potential of the next generation nuclear energy systems [6]. The initiative has four goals defined in the GIF charter. The first goal is sustainability, to produce energy sustainably and promote long-term availability of nuclear fuel, while minimizing nuclear waste and reducing the long stewardship burden. The other goal is to excel in safety and reliability, by having a very small likelihood and degree of reactor core damage and eliminating the need for off-site emergency response. The GIF charter's other objective is with regards to economics, to have a life cycle cost advantage over other energy sources and to have a level of financial risk comparable to other energy projects. Last but not least is the objective of proliferation resistance and physical protection, to be a very unattractive route for diversion or theft of weapon-usable materials, and provide increased physical protection against acts of terrorism. Below two types of advanced reactors, namely the high-temperature-gas-cooled reactors and the accelerator-driven reactors are discussed on how they answer to the stipulated goals.

3.3.1 High-Temperature Gas-Cooled Reactors

High-Temperature Gas-Cooled Reactors (HTGR) are a special design different from the ordinary design of nuclear reactors. They are based on the pebble bed modular design (figure 3.4) with a different arrangement and design of fuel. The fuel is of spherical design instead of rods/pellets and uses helium gas as a coolant. The reactor core can be operated at temperatures close to the fuel's melting point thereby increasing the overall heat extraction. The design has not yet been tested commercially, but is projected to have efficiency of 15% more than the commercially used LWR [2]. The HTGR fuel design is a graphitic Tri-structural Isotropic (TRISO) sphere design (figure 3.5) used to contain all the fission products without leakage.

The sphere contains a kernel that hosts a low enriched uranium oxide (UO_2) fuel beyond the temperature of 1600^0C given any accidental scenario. It contains pyrolitic carbon (PyC) layers for barrier. The barrier layers include the porous carbon buffer used to reduce the force of the recoils from the fission products released during fission reactions and provides a porous escape for the fission gases. The next layer is that of the inner denser PyC carbon used to retain the fission gases led through the porous carbon buffer. Then following this layer is the ceramic layer that provides structural integrity to the fuel made of SiC and retains fission products at high temperatures. The last layer is that of the outer layer PyC which provides protection to the ceramic layer against the wearing conditions of the nuclear environment. Table **??** shows the dimensions and properties of the different layers for the design of the TRISO particle.

The TRISO fuel particle has a very large surface area to allow maximum heat transfer to the coolant (helium). Helium gas is allowed to flow through the pebble bed and transfers the heat from the fuel particle through a heat exchanger to heat the water to produce steam. The TRISO particle is designed to accommodate all the fission gases and products generated during high burn-up.

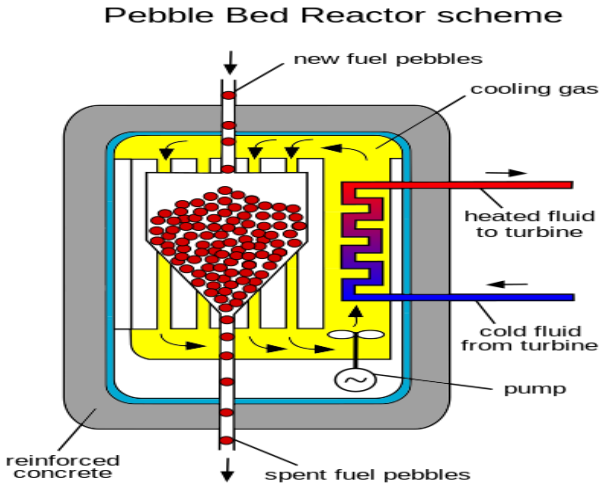

Figure 3.4: *Pebble bed reactor design [7]*

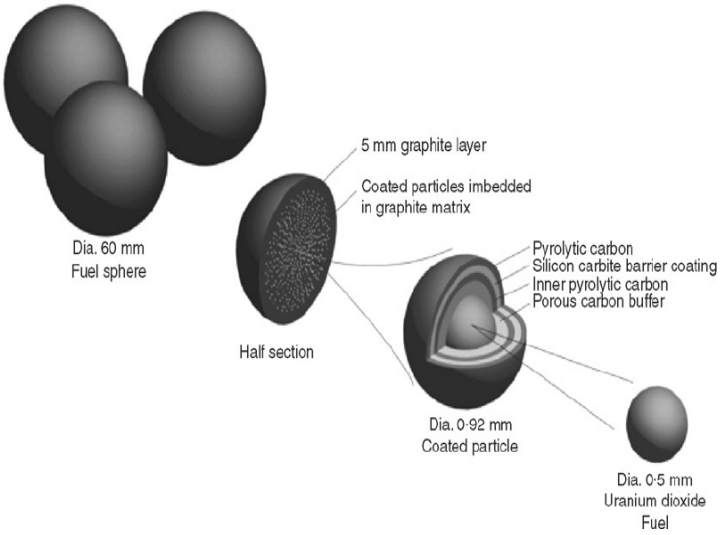

Figure 3.5: *TRISO fuel element design [8].*

Table 3.2: TRISO particle dimensions and properties [9]

	Thickness (μm)	Ultimate Tensile Stress (MPa)	Young's Modulars (GPa)	Poisson's Ratio	Density (g/cm^3)
Kernel	(Radius) 165				
Buffer	73				
Inner PyC	10	344	668	0.24	15.8
SiC	67	200	410	0.14	6.73
Outer PyC	15	344	668	0.24	15.8

3.3.2 Accelerator-Driven Reactors

The Accelerator Driven System (ADS) is a type of advanced nuclear reactor that maintains power generation without reaching criticality. For a nuclear reactor to reach criticality the amount of generated neutrons from fission reactions should be in equilibrium with the amount being absorbed within the reactor and those lost through leakage. This equilibrium helps the reactor to keep power at a required level. ADS reactors generate less neutrons from fission reactions than those absorbed by different materials in the reactor and those lost via leakage, hence they operate at sub-critical levels. To keep power at any required level in the ADS reactor, external neutrons are supplied from the reaction of a high energy proton beam with a heavy nucleus such as lead by spallation. The fissile fuel is irradiated with neutrons in a reactor

environment and spallation multiplies these neutrons and supply them for transmutaion and capture [10].

The spallation process involves the reaction of high-energy protons from an accelerator with a target material to discharge neutrons with reduced energy. The nucleus may 'boil-off'the neutrons to reach the ground state. Close to 90% of the neutrons generated in the ADS reactor are due to the 'boil-off' by spallation. The accelerator is powered by fission events and drives the reactions and therefore expelling the need for control rods in the fuel configuration. The stronger the external sources the greater the power levels in the ADS reactors. These reactors are designed and developed to burn radioactive nuclear waste generated that would otherwise retain their radio-toxicity for millions of years. They are designed to produce reliable energy while reliably transmuting waste to stable elements, or to those with a reasonably short radioactivity lifetime. The United States and Japan are highly involved in research and development of these ADS reactors [10, 11, 12, 13, 14, 15, 16].

Bibliography

[1] Shultis, J.K., and Faw, R.E., (2002). *Fundamentals of nuclear science and engineering*, CRC press, United States

[2] Sekimoto, H., (2007). *Nuclear reactor theory*, COE-INES Tyoko Institue of Technology

[3] Singhai, R.K., Narayanan, U., Karpe, R., Kumar, A., Ranade, A.,and Ramachandran, V., (2009). 'Selective separation of iron from uranium in quantitative determination of traces of uranium by alpha spectroscopy in soil/sediment sample'. *Applied Radiation and Isotopes*, 67(4), pp. 501-505

[4] Soppera, N., Bossant, M., Dupont, E., (2014). 'JANIS 4: An Improved Version of the NEA Java-based Nuclear Data Information System'. *Nuclear Data Sheets*, 120, pp. 294-296

[5] Banerjee, S., and Gupta, H.P., (2009). *Nuclear Power from Thorium: Some Frequently Asked Questions*, Nayak A., Sehgal B. (eds), Thorium—Energy for the Future. Springer, Singapore

[6] Generation IV International Forum, (2019). *GEN IV International Forum*. Accessed 17 June 2019, `https://www.gen-4.org/gif/jcms/c_9260/public`

[7] Errymath, (2016). *Pebble-bed reactor: Meltdown-Proof Nuclear Reactor*. Accessed 18 June 2019, `http://errymath.blogspot.com/2016/02/pebble-bed-reactor-meltdown-proof.html#.XQjnArozbeQ`

[8] Ion, S., Nicholls, D., Matzie, R., and Matzner, D., (2004). 'Pebble bed modular reactor-the first Generation IV reactor to be constructed'. *Nuclear Energy*, 43(1), pp. 55-62

[9] Stacey, W.M., Boakye, K.A., Brashear, S.K., Bryson, A.C., Burns, K.A., Bruch, E.J., Chandler, S.A., Chen, O.M., Chiu, S.S., Floyd, J-P., Fong, C.J., Hamilton, S.P., Johnson, P.B., Jones, S.M., Kato, M., MacLaren, B.A., Manger, R.P., Merriweather, B.L., Mitra, C., Riggs, K.R., Shrader, B.H., Schulz, J.C., Sommer, C.M., Sumner, T.S., Wagner, J.S., Weathers, J.B., Wells, C.P., Willis, F.H., Friis, Z.W., Marquez-Danian, J.I., Johnson, R.W., de Oliveira, C., Park, H.K., and Tedder D.W., (2007). 'Advances in the Subcritical, Gas-Cooled, Fast Transmutation Reactor Concept'. *Nuclear Technology*

[10] Kurata, Y., Takizuka, T., Osugi, T., and Takano, H., (2002). 'The accelerator driven system strategy in Japan'. *Journal of Nuclear Materials*, 301(1), pp. 1-7

[11] Beller, D.E., Van Tuyle, G.J., Bennett, D., Lawrence, G., Thomas, K., Pasamehmetoglu, K., Li, N., Hill, D., Laidler, J., and Fink, P., (2001). 'The US accelerator transmutation of waste program'. *Nuclear Instruments & Methods In Physics Research Section A-Accelerators Spectrometers Detectors and Associated Equipment*, 463(3), pp. 468-486

[12] Eremeev, I.P., (1995). 'Accelerator-based gamma neutron transmutation of radionuclides as a new technology for the nuclear fuel cycle'. *Proceedings Particle Accelerator Conference*, Dallas, TX, USA, USA, (1-5 May 1995)

[13] Tsujimoto, K., Sasa, T., Nishihara, K., Takizuka, T., and Takano, H., (2000). 'Accelerator-driven system for transmutation of high-level waste'. *Progress in Nuclear Energy*, 37(1-4), pp. 339-344

[14] Sasa, T., Nishida, T., Takizuka, T., Sato, O., and Yoshizawa, N., (1998). 'Neutronics and burnup analysis of an accelerator-based tru-nitride fuel transmutation system with the ATRAS code'. *Progress in Nuclear Energy*, 32(3-4), pp. 485-490

[15] Tsukada, K., Nishinaka, I., Shinohara, N., Ichikawa, S., Nagame, Y., Sueki, K., Nakahara, H., Ohtsuki, T., Tanikawa, M., (1998). 'Fragment mass dependence of angular anisotropy in 15 MeV proton-induced fission of ^{244}Pu'. *The European Physical Journal A*, 2(2), pp.153-155

[16] Kim, Y.S., Hofman, G.L., (2001). *AAA Fuels handbook*, United States

Chapter 4

Ion implantation and Irradiation

When energetic ions impinges on a substrate, they interact with the target nucleus and electrons. During the interactions, the ions lose energy through collisions with the target nucleus and electrons and until they come to rest at some depth within the target. This process is called ion implantation. The type of incident ion, substrate material, and the accelerating energy determines the typical depth where ions come to rest. Ion implantation energies range from a few keV to MeV. This chapter presents the theory of ion irradiation and implantation. The chapter also present Xenon and Europium as fission products, and the SRIM simulation.

4.1 Ion Irradiation

4.1.1 Ion Stopping

Figure 4.1 is a schematic of energetic incident ions penetrating a target. The energetic ions encounter a chain of collisions with the host atoms and electrons. During these collisions, they lose their energies until they come to rest at some depth inside the target. The depth at which the ions come to rest depends on the ion's initial incident energy. The initial energy of ions may range from few keV to MeV. In the low energy range the ion's energy is mainly lost via collision with the target atoms (elastic collision termed nuclear energy loss) while in higher energy range the energy loss is via the interactions with the electrons (inelastic collision termed electronic energy loss). Therefore, the total energy loss is a combination of electronic and nuclear energy losses until the ion comes to rest at a particular depth. Thus, the stopping

power S, characterized by the energy loss (E) per unit path length (x) of the ion, is the sum of these energy loss factors.

$$S = \left(\frac{\partial E}{\partial x}\right)_{Nuclear} + \left(\frac{\partial E}{\partial x}\right)_{Electronic} \tag{4.1}$$

The relative distribution of S for each of the terms over a wide range of energies is shown in figure 4.2. Energies normal for ion implantation, 10 to 200 keV, fall at the most distant left of the curve, a locality governed by nuclear stopping. The impact between two atoms is the source of nuclear stopping, and this can be portrayed by classical kinematics [1]. If these atoms are assumed to be nuclei, and given the separation between them of r, the coulombic potential between them would be given by

$$V_c(r) = \frac{q^2 Z_1 Z_2}{4\pi\epsilon_0 r} \tag{4.2}$$

where Z_1 and Z_2 are the atomic numbers of the implanted and target atoms, respectively, ϵ_0 is the permittivity, and q is the electronic charge. In actuality, electrons screen the nuclear charge and a screening function $f_s(r)$, must be included such that

$$V(r) = V_c(r) f_s(r) \tag{4.3}$$

Given an energetic ion of mass M_1 and velocity v_0 and therefore energy E_0 is given by

$$E_0 = \frac{1}{2} M_1 {v_0}^2 \tag{4.4}$$

The atom of mass M_2 with which the ion will collide is initially at rest. Velocities v_1 and v_2 and the energies E_1 and E_2 of the incident ion and the target atoms, respectively, will after collision be given by the scattering angle θ and the recoil angle ϕ as shown in figure 4.3. From the conservation of energy and momentum in the center-of-mass frame, the energy transfer by the incoming ion to the target atom, T, is given as follows [1]

$$T = E_2 = \frac{4M_1 M_2}{\left(M_1 + M_2\right)^2} E_0 \sin^2\left(\frac{\theta}{2}\right) \tag{4.5}$$

Therefore, the rate of energy loss by nuclear collisions, S_n, per unit path length can be calculated by summing the energy loss multiplied by the probability of that collision occurring, and

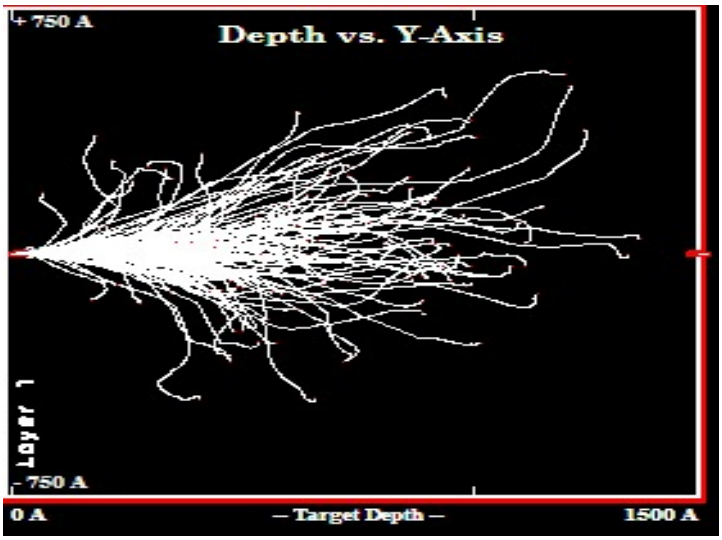

Figure 4.1: *Monte Carlo calculation of 128 ion trajectories for 360 keV Xe implanted into ZrN*

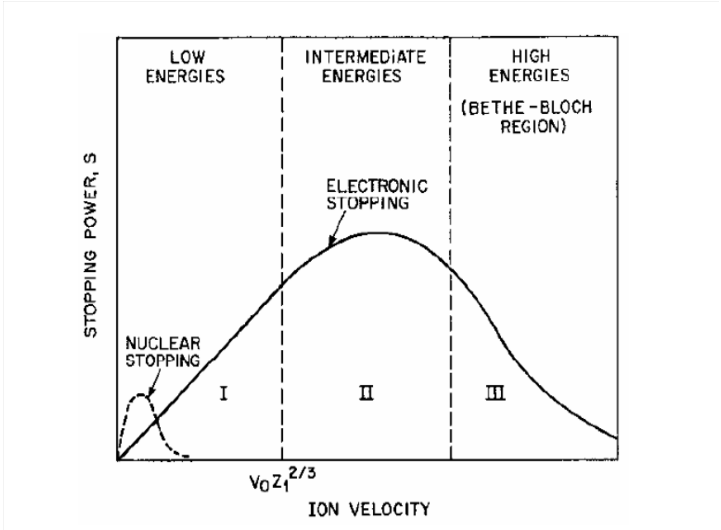

Figure 4.2: *Nuclear and electronic components of the ion stopping power as a function of ion velocity. The quantity v_0 is the Bohr velocity, $\frac{q^2}{4\pi\epsilon_0\hbar}$, and Z_1 is the ion atomic number [2].*

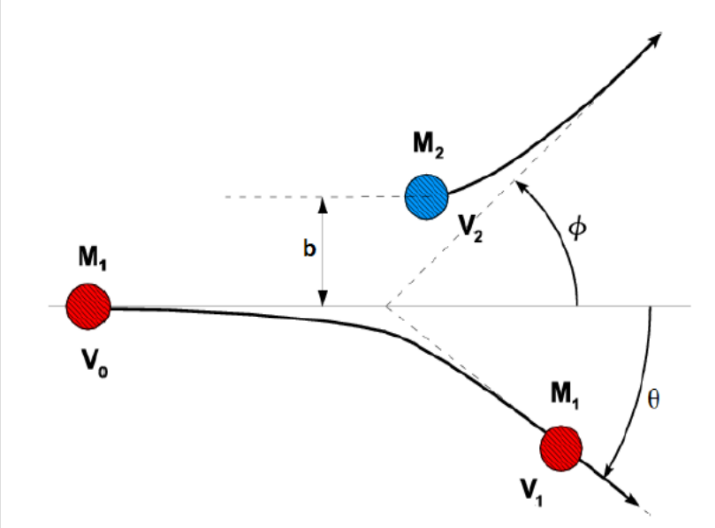

Figure 4.3: *Illustration of an elastic collision defining the various velocities involved before and after collision [3].*

it is given by

$$S_n = \left(\frac{\partial E}{\partial x}\right)_{Nuclear} = N \int_0^{T_max} T d\sigma, \tag{4.6}$$

where $d\sigma$ is the differential cross-section. Nuclear stopping is elastic and energy loss by the incident ion is transferred to the target atom that is consequently recoiled away from its lattice site, thus creating a damage or defect site. For ions with kinetic energies less than $100\,keV/nucleon$, energy loss will be through the nuclear energy loss mechanism.

The interaction of charged particles is a necessary part of electronic stopping. At high energies, the charge state of the ion increases up to a point where it becomes totally vacant of every one of its electrons where the velocity $v \geq v_0 {Z_1}^{\frac{2}{3}}$ [1]. The ion can be taken as a positive point charge Z_1 at this point, moving with a velocity greater than the orbital velocity of the atomic electrons of the target molecules. With the high-velocity conditions, the interaction of the ion with the target molecules can be taken as a small and sudden exterior perturbation, delivering energy transfer from the ion to the target electron [1]. The energy loss from a swift ion to a nucleus or electron can be determined by means of scattering theory in a central field [4]. As the velocity of the ions increases the stopping cross-section decreases because the ions spends less time near the vicinity of the atoms.

4.1.2 High and Low Electronic Energy Loss

The incident ion can be viewed as a positive point charge Z_1, if the ion's velocity is much greater than $v_0 {Z_1}^{2/3}$. The energy in this circumstance is given by

$$-\frac{dE}{dx}\Big|_e = \frac{2\pi {Z_1}^2 e^4}{E_0} N Z_2 \Big[\frac{M_1}{m_e}\Big] \ln \frac{2m_e v^2}{I}, \tag{4.7}$$

where m_e is the mass of the electron, N is the atomic density, M_1 the mass of the incident charged particle, v is the velocity of the particle and the rest are as defined above. The average excitation energy I in electron volts is given as

$$I \cong 10 Z_2 \tag{4.8}$$

where Z_2 is the atomic number of the target atom. The depiction of stopping power up to this point disregards the shell structure of the atoms and different electron bonds.

In the circumstance where $v < v_0$, eq. 4.7 is no longer legitimate. For energetic charged particles moving with a velocity $v < v_0 {Z_1}^{2/3}$, the velocities of most of the atomic electrons are more prominent than that of the incident particles. In this circumstance, the electrons can't pick up energy from the ions through direct impact. Firsov [6] created a model portraying this which includes the exchange of momentum when the target electrons are caught by the particle. For this to happen the electron should be accelerated to the particle velocity v. Through this procedure the particle loses a little measure of momentum relative to $m_e v$. In addition to Firsov's model, Lindhard and Scharff [7] also produced a model and can likewise be acquired through the strategy followed by Firsov. The essential contrast between these models lies in the choice of interaction potential. The Lindhard-Scharff stopping cross-section is given by

$$S_e(E) = 3.83 \frac{{Z_1}^{7/6} Z_2}{\left({Z_1}^{2/3} + {Z_2}^{2/3}\right)^{3/2}} \Big[\frac{E_0}{M_1}\Big]^{1/2} = K_L E^{1/2} \tag{4.9}$$

where K_L is the Lindhard-Scharff constant and all the other terms are as defined above.

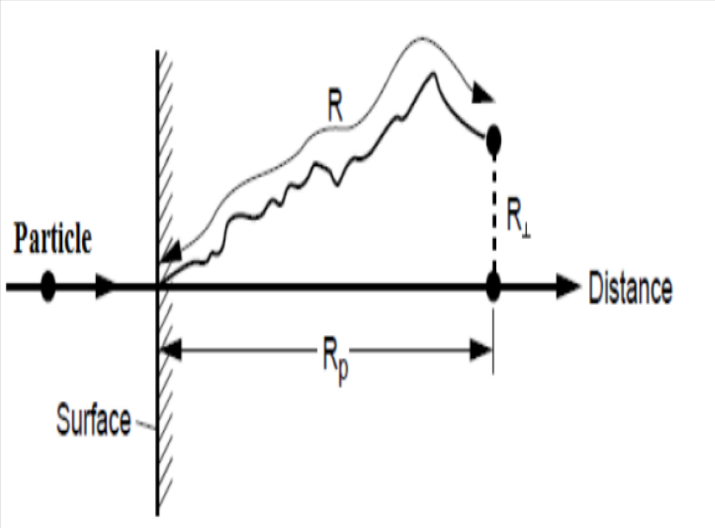

Figure 4.4: *A particle incident on a solid penetrated with a total path length R, resulting in a projected range Rp, along the direction parallel to the incident ion [7].*

4.1.3 Ion Range

Incident ions lose energy by means of nuclear and electronic interactions with the target atoms, as already mentioned above. Nuclear interactions are described by individual elastic collisions between the incident ion and the target atoms, whereas electronic interactions can be depicted as a continuous viscous pull phenomenon between the incident ions and the sea of electrons around the target atoms [1].

The path taken by the ions as they come to rest inside the target atoms is presented in figure 4.4. R is the range, the total distance covered by the embedded ions. R_p on the other hand is the penetration depth, the net ion penetration depth in the solid. It is the perpendicular distance to the surface of the sample measured to the point where the ions come to rest. As the implanted ions penetrate the solid, they lose energy and the rate of this energy loss along the path of the ions determines the range, given by

$$R = \int_{E_0}^{0} 1/\frac{\partial E}{\partial x} dE \tag{4.10}$$

where E_0 is the incident energy of the implanted ion.

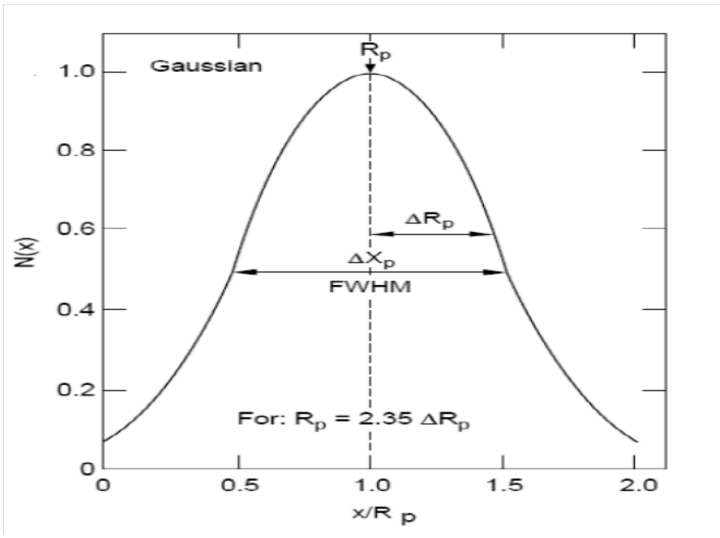

Figure 4.5: *Gaussian range distribution for implanted particles with* $R_p = 2.35\Delta R_p$ *and a full width half-maximum of* ΔX_p *[7].*

4.1.4 Ion Distribution

Ion stopping by a solid is a random process because of the collision succession; particle avoidance and the total path length fluctuates arbitrarily from particle to particle. Consequently, ions of similar energy and angle of incidence in the target material would lag over a scope of various depths with the most plausible projected range alluded to as the average or mean projected range. Figure 4.5 shows the depth distribution $N(x)$, normalized for a fluence of ϕ_i, given by

$$N(x) = \frac{\phi_i}{(2\pi)^{1/2}\Delta R_p} e^{\left(\frac{-1}{2}\right)\left(\frac{x-R_p}{\Delta R_p}\right)^2} \tag{4.11}$$

where R_p is the projected range (mean depth of the distribution) and ΔR_p is the projected range straggling (standard deviation of the distribution) [10].

Ref [9] developed the analytical approach used to get range quantities and is referred to as the LSS theory. With a precision of around 20 %, it allows for the computation of range values.

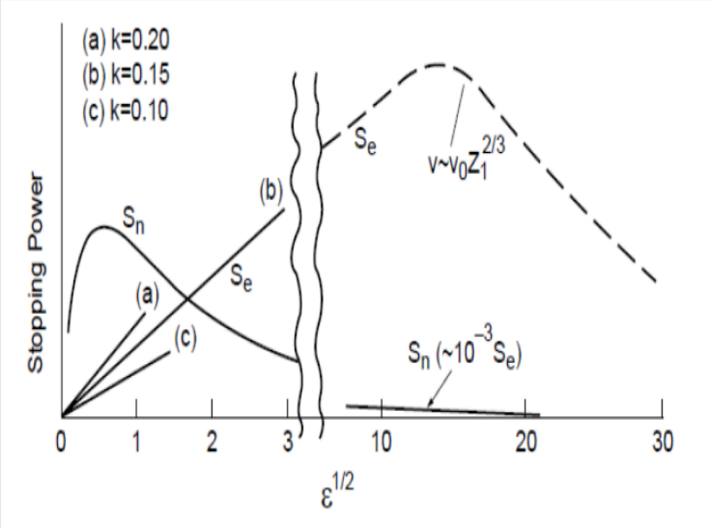

Figure 4.6: *Nuclear and electronic stopping powers in reduced units. The electronic stopping power variable k is dependent on the mass and atomic number of the incident particle and the atoms of the target [7].*

4.1.5 The LSS Theory

From the Thomas-Fermi (TF) statistical model of the interaction between heavy particles [11], the theory determines an all-inclusive nuclear stopping power S_n, and an electronic stopping power S_e corresponding to the velocity, v, of the projectile. The potential is of the form

$$V(r) = \frac{Z_1 Z_2 e^2}{4\pi\epsilon_0 r}\phi\Big(\frac{r}{a}\Big), \tag{4.12}$$

where, $a = \frac{a_0}{\left({Z_1}^{2/3}+{Z_2}^{2/3}\right)^{1/2}}$ and ϕ are the TF screening functions estimated by

$$\phi\Big(\frac{r}{a}\Big) = \left(\frac{r/a}{\left(r^2/a + c^2\right)^{1/2}}\right), \tag{4.13}$$

where $c = \sqrt{3}$ giving a better average fit to the Thomas-Fermi potential. The theory predicts a nuclear stopping power $S_n(E)$ of the shape in figure 4.6, utilizing approximation methods.

The terms ϵ and ρ are dimensionless quantities in the model representing energies and distances, respectively, and they are given as [14]

$$\epsilon = E\frac{aM_2}{Z_1 Z_2 e^2\big(M_1 + M_2\big)} \tag{4.14}$$

$$\rho = RN4\pi a^2 \frac{M_1 M_2}{\big(M_1 + M_2\big)^2} \tag{4.15}$$

From these quantities, we find the nuclear stopping power S_n, i.e. $\left\{\frac{d\epsilon}{d\rho}\right\}_n$ as an element of ϵ alone and free of the incident particle or target material with the end goal that figure 4.6 speak to a universal stopping power. In like manner, the electronic stopping S_e is given by [16]

$$\left\{\frac{d\epsilon}{d\rho}\right\}_e = ke^{1/2} \tag{4.16}$$

such that

$$k = \xi_e \frac{0.0793{Z_1}^{1/2}{Z_2}^{1/2}\big(M_1 + M_2\big)^{3/2}}{\big({Z_1}^{2/3} + {Z_2}^{2/3}\big)^{3/4}{M_1}^{3/2}{M_2}^{3/2}} \tag{4.17}$$

where

$$\xi_e \approx {Z_1}^{1/6} \tag{4.18}$$

and k relies upon the approaching particle, and in this way, a general curve for the electronic stopping can't be accomplished. Whenever $Z_1 > Z_2$, k is of the order $0.1 - 0.2$ and just when $Z_1 \ll Z_2$ does k ends up noticeably more than 1. At this point, the mean path length can be calculated from

$$\rho = \int_0^{\epsilon} \frac{d\epsilon}{S_n(\epsilon) + S_e(\epsilon)} \tag{4.19}$$

4.1.6 Europium and Xenon as Fission Products

Nuclear fission processes release various radioactive and non-radioactive fragments of different mass numbers around 90 and 140 [13]. Europium is one of the fragments released in the nuclear fission processes. However, europium and its isotopes have low fission product yield. ^{151}Sm beta decays into ^{151}Eu, however ^{151}Sm has a long decay half-life and short neutron absorption mean time leading to nearly all of it turning to ^{152}Sm. ^{152}Sm and ^{154}Sm are not

radioactive and would therefore not beta decay into either ^{152}Eu or ^{154}Eu "shielded nuclides", because they are formed as primary products of some nuclear transformation like fission and not beta decay and ^{154}Eu is the only long-lived one other than ^{134}Cs to have a fission yield of more than 2.5 ppm [14]. Most of the ^{154}Eu is generated as a result of neutron activation of non-radioactive ^{153}Eu even so much of it to a greater extend is transmuted to ^{155}Eu, which has 330 ppm fission yield of ^{235}U and thermal neutrons. Much of the ^{155}Eu is further converted to a non-radioactive and absorption-resistant ^{156}Gd by the end of the burn-up [15].

Xenon and its isotopes is another one of the fragments produced by nuclear fission processes [16, 26]. During the fission processes ^{135}Te is produced which then beta decays into a 6.7 hours half-life ^{135}I. The short half-life and low neutron capture of ^{135}I leads it to beta-decay into a high neutron absorber with a cross-section of 2.6×10^6 *barns*, ^{135}Xe. Xenon has about nine isotopes and only seven of these are radioactive. ^{135}Xe has a 5% chance of being generated from each fission reaction with 95% chance from ^{135}I beta-decay and has a half-life of 9.1 hours [18, 19]. If the concentration of ^{135}Xe increases in the reactor, the neutron concentration will decrease due to the absorption by high cross-sectional ^{135}Xe. This could lead to a reactor shutdown, unless this absorption stimulates transmutation to stable ^{136}Xe. The reactor shutdown could cause ^{135}Xe poisoning (figure 4.7). This causes a substantial decrease in reactivity (neutron flux) in just 10 hours of the reactor shutdown (curve 2 in figure 4.7). Since ^{135}I has a half-life of 6.7 hours, it quickly beta-decays and increases the concentration of ^{135}Xe (curve 1 in figure 4.7) and thus the poisoning. It would not be possible to restart the reactor once the reactor reaches a xenon dead time. Therefore, since ^{135}Xe has a half-life of 9.1 hours, the poison should be left to decay for a couple of days before the reactor could be restarted.

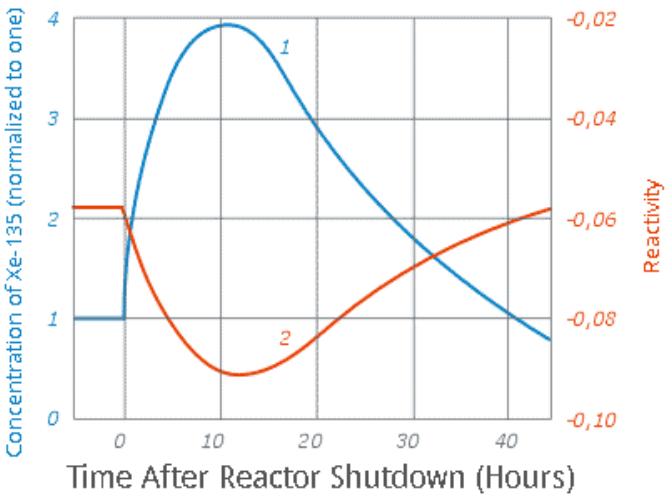

Figure 4.7: *Concentration of* ^{135}Xe *after the reactor shutdown [20].*

4.2 SRIM Simulation

SRIM (Stopping and Range of Ion in Matter) [27] is a Monte-Carlo simulation software that calculates the interaction of ions in matter. In this study, the 2012 version of SRIM was used in the simulation of Xe and Eu ion implantation on ZrN. The SRIM simulation is not dependent on the fluence of the ions and does not take into account the crystal structure or dynamic compositional change in the target as a result of the impinging ions. The simulation however is based on a few approximations to make its calculations, and those include:

- binary collision, that is the influence of neighbouring atoms is not taken into account;
- recombinations of knocked off atoms (interstitials) with the vacancies is also not considered;
- the electronic stopping power is an averaged fit to a large number of experiments;
- the inter-atomic potential as a universal form which is an averaging fit to quantum mechanical calculations;
- the target atom which reaches the surface is able to leave the surface (be sputtered) if it has sufficient momentum and energy to pass the surface barrier

The SRIM Monte Carlo simulation of ion recoils generated by the nuclear collisions (full cascade damage) of 360 keV Eu and Xe ions as well as 167 MeV Xe ions in ZrN is shown in figure 4.8. The displacement energies used for Zr and N atoms are 35 and 25 eV respectively [1] The simulation shows a higher deposited energy density for all the ions as expected for heavy ions, with the low-energy implantation showing similar damage and high-energy irradiation showing high deposited energy density deeper into the samples. The implantation damage is a function of mass ratio of incident ion to target atoms, energy, fluence, fluence rate and temperature.

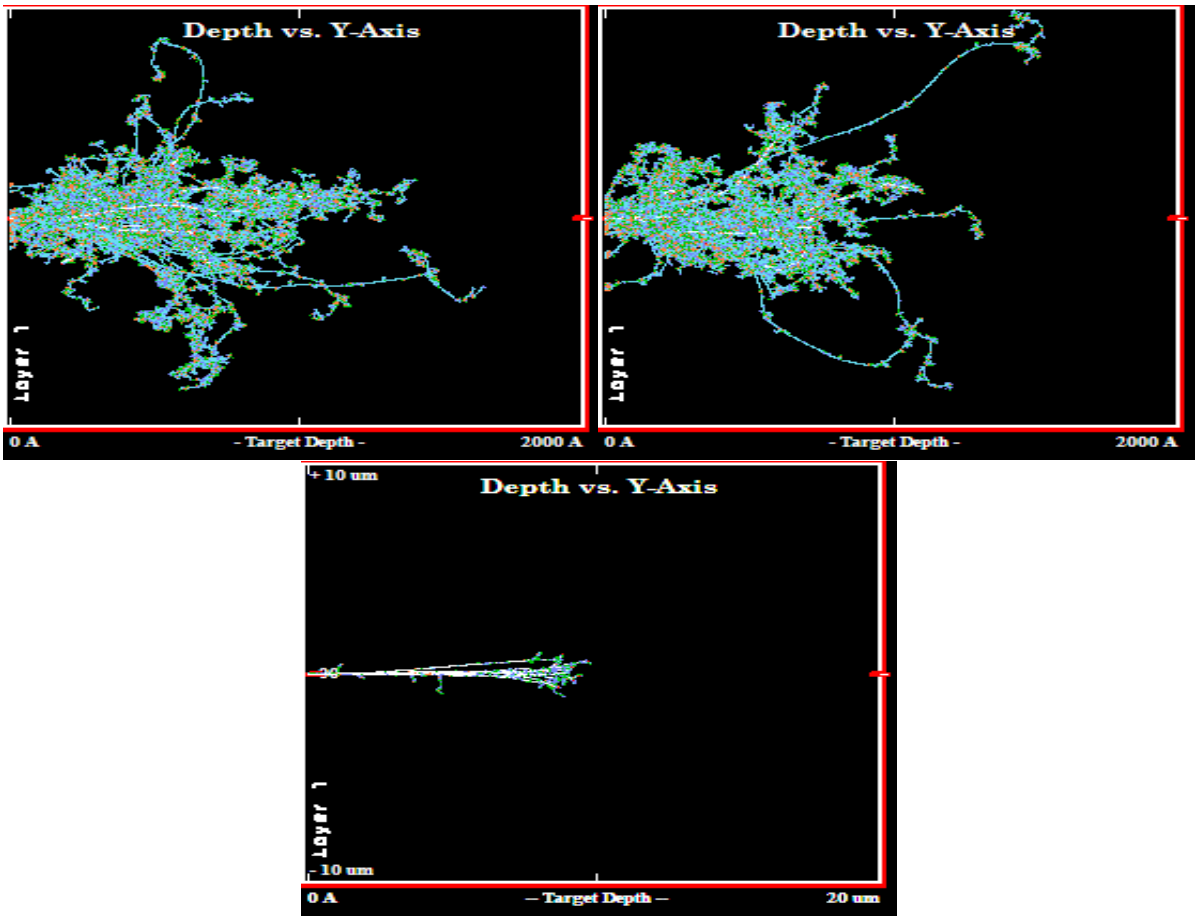

Figure 4.8: *SRIM Simulation showing full cascades for 10 incident ion tracks in ZrN for Xe (top left) and Eu (top right) of 360 keV and Xe of 167 MeV (bottom)*

The number of times an atom is dislodged for a given fluence is called displacement per atom (dpa). It is used to compare radiation damage by different ions at different fluences. Change in

material properties is given as a function of the displacement per atom, and can be calculated as,

$$dpa\left(\frac{vacancy}{atoms}\right) = \frac{total\ fluence(ions/cm^2) \times vacancy\left(\frac{vacancies}{ion\,\mathring{A}}\right) \times 10^8}{atomic\,density(atoms/cm^3)} \tag{4.20}$$

Assuming that none of the implanted ions are lost during implantation/irradiation, the relative atomic density(%RAD) of the implanted ions in the bulk (ZrN in this case) can be calculated. First the density ($\rho_{implanted\,ion}$) of the implanted ion is calculated from the total counts/distribution and the fluence (ϕ) at which it is implanted as,

$$\rho_{implanted\,ion} = fluence(\phi)(ions/cm^2) \times ion\,distribution(ions/cm) \tag{4.21}$$

Now to get the relative atomic density of the implanted ions, we need to also find the atomic density of the bulk (ρ_{bulk}) in $atoms/cm^3$, and therefore find the ratio of the two densities as,

$$RAD(\%) = \frac{\rho_{implanted\,ions}}{\rho_{bulk}} \times 100\% \tag{4.22}$$

where $\rho_{implanted\,ions}$ is ρ_{Eu} or ρ_{Xe} and ρ_{bulk} is $\rho_{ZrN} = 8.2638 \times 10^{22} atoms/cm^3$ in this study using the ZrN density of $7.22\ g/cm^3$.

Bibliography

[1] van Vuuren, A.J., (2014). *Swift Heavy Ion Radiation Damage in Nanocrystalline ZrN* (Doctoral dissertation, Nelson Mandela Metropolitan University)

[2] Machaka, R., (2006). 'Ion Beam Modifications of Boron Nitride By Ion Implantation'(Doctoral dissertation).

[3] Micelotta, E.R., Jones, A.P. and Tielens, A.G.G.M., (2010). 'Polycyclic aromatic hydrocarbon processing in interstellar shocks'. *Astronomy & Astrophysics*, 510, p.A36.

[4] (2007) 'APPENDIX C.QUANTUM THEORY OF SCATTERING BY A CENTRAL POTENTIAL'. *Journal of the International Commission on Radiation Units and Measurements*, 7(1), pp.131-149

[5] Oguri, Y., Niinou, T., Nishinomiya, S., Katagiri, K., Kaneko, J., Hasegawa, J. and Ogawa, M., (2007). 'Firsov approach to heavy-ion stopping in warm matter using a finite-temperature Thomas–Fermi model'. *Nuclear Instruments and Methods in Physics Research Section A: Accelerators, Spectrometers, Detectors and Associated Equipment*, 577(1-2), pp.381-385.

[6] Lindhard, J., Scharff, M. and Schiøtt, H.E., (1963). 'Range concepts and heavy ion ranges'. *Copenhagen: Munksgaard.*

[7] Nastasi, M.A. and Mayer, J.W., (2006). 'Ion implantation and synthesis of materials'(Vol. 80). Berlin: Springer.

[8] Jahnel, F., Ryssel, H., Prinke, G., Hoffmann, K., Muller, K., Biersack, J. and Henkelmann, R., (1981). 'Description of arsenic and boron profiles implanted in SiO2, Si3N4 and Si using Pearson distributions with four moments'. *Nuclear Instruments and Methods*, 182, pp.223-229.

[9] Lindhard, J., Scharff, M. and Schiøtt, H.E., (1963). 'Range concepts and heavy ion ranges'. Copenhagen: Munksgaard.

[10] Feenberg, E., (1937). 'A Note on the Thomas-Fermi Statistical Method'. *Physical Review*, 52(7), p.758.

[11] Tsurushima, T. and Tanoue, H., (1971). 'Spatial distribution of energy deposited by energetic heavy ions in semiconductors'. *Journal of the Physical Society of Japan*, 31(6), pp.1695-1711.

[12] Thomas, J. ed., (2012).*Material characterization using ion beams* (Vol. 28). Springer Science & Business Media.

[13] Tayal, D.C., (2009). *Nuclear Physics*, Himalaya Publishing House

[14] Japan atomic energy agency, (2015). *Tables of Nuclear data*, archived 10 June 2015

[15] Hordosy, G., (2003). 'Studies of the influence of the spatial change of the fuel burnup on criticality in WWER-440 systems'. *Practices and developments in spent fuel burnup credit applications*, p.148.

[16] Wolfsberg, K., (1965). 'Nuclear Charge Distribution in Fission: Fractional Yields of Krypton and Xenon Isotopes from Thermal Neutron Fission of U 233 and Pu 239 and from 14-MeV Neutron Fission of U 235 and U 238'. *Physical Review*, 137(4B), p.B929.

[17] Wahl, A.C., (1958). 'Nuclear-charge distribution in fission: Cumulative yields of short-lived krypton and xenon isotopes from thermal-neutron fission of 235U'. *Journal of Inorganic and Nuclear Chemistry*, 6(4), pp.263-277.

[18] U.S. Department of Energy, DOE Fundamentals Handbook, DOE-HDBK-1019, (1993). *Nuclear Physics and Reactor Theory*, Vol. 1 and Vol. 2

[19] Stacey, W.M., (2007). *Nuclear Reactor Physics*, 2nd edn, Wiley-VCH

[20] Alnoaimi, K., (2014). *Xenon-135 Reactor Poisoning*, Stanford University. ¡`http://large.stanford.edu/courses/2014/ph241/alnoaimi2/`¿

[21] Ziegler, J.F., Biersack, J.P., Ziegler, M.D., (2012). 'SRIM2008-The Stopping and Range of Ions in Matter', SRIMCo.,Chester

[22] Jiao, L., Yu, K.Y., Chen, D., Jacob, C., Shao, L., Zhang, X. and Wang, H., (2015). 'Radiation tolerant nanocrystalline ZrN films under high dose heavy-ion irradiation'. *Journal of Applied Physics*, 117(14), p.145901.

Chapter 5

Experimental Techniques

There are a few analytical techniques used to characterize radiation damage in materials. This chapter presents the techniques used for the analysis of damage in ZrN. The chapter is divided into the following subsections. The first is the Raman spectroscopy as the primary analytical technique used to determine any surface, phase and structural changes due to radiation damage. Rutherford backscattering spectrometry (RBS) is also presented as a technique used to study the migration behaviour of europium (Eu) in ZrN. The cross-sectional scanning electron microscopy (SEM) is presented as the tool used to determine the thickness of deposited ZrN layers. The other subsection deals with grazing incidence x-ray diffraction (GIXRD) as a technique used to determine phase changes and crystalline size due to radiation induced damage.

5.1 Raman Spectroscopy

Raman spectroscopy is an analytical tool used in chemistry and material science to determine vibrational modes of molecules [2]. The technique depends on inelastic scattering of phonons. This technique is also based on the theory of Raman effect, which deals with what happens when monochromatic light interacts with a molecule. This section discusses the Raman spectroscopy theory focusing on the classical theory (subsection 5.1.1.1), quantum theory (subsection 5.1.1.2) and the selection rules (subsection 5.1.1.3) of the Raman effect.

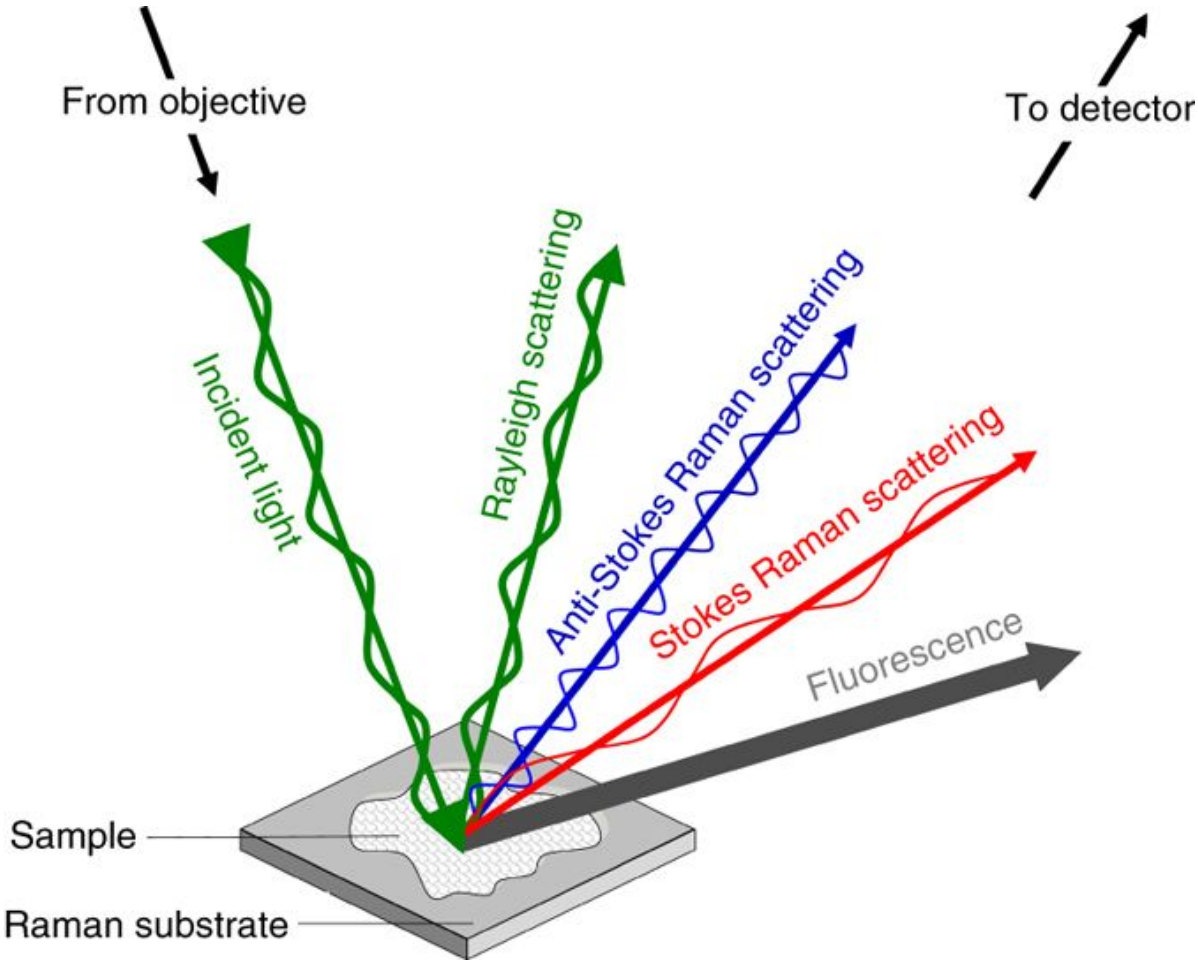

Figure 5.1: *Schematic representation of different Raman scattering that arise from a monochromatic laser incident beam on a specimen (Adopted from: (Curtis et al., 2016) [5]).*

5.1.1 Raman effect

When a monochromatic laser beam is irradiated on a specimen, the vast majority of the scattered light is scattered elastically with a frequency equivalent to the incident monochromatic light. Rayleigh scattering is the elastic light scattering phenomenon which is more than 99% of all the scattered light [1]. A Raman spectrum is developed from the less than 1% of the scattered photons (inelastic scattering). This scattering is due to the inelastic collisions between the incident monochromatic light and the particles of the specimen [4].

The inelastic scattering of incident photons can either lose energy (Stokes; resulting scattered

light has lesser frequency than the incident light) or gain energy (anti-Stokes; the resulting scattered light has higher frequency than the incident light (figure 5.1)) [6]. Also in figure 5.1, incident monochromatic photons can be reflected without any interaction with the specimen (fluorescence). This happens mostly in materials with metallic properties.

5.1.1.1 Classical theory of Raman effect

The classical theory of Raman scattering is a take on the aspect of polarizability of electron clouds around molecules. According to the theory, when molecules are in an electric field, they experience a change in the distribution of the electron cloud around them. The electrons will be attracted to the positive end of the field while the positive nucleus will move towards the negative end of the field. The splitting of the charges results in an induced dipole moment. The product of the polarizability of the molecule α, and the electric field strength E, of the laser beam is directly proportional to the induced dipole moment, μ.

$$\mu = \alpha \cdot E \tag{5.1}$$

This dipole moment depends on the distortion of the electron cloud which can be characterized as an ellipsoid. Therefore, the oscillating electric field strength will result in an oscillating dipole moment. This oscillating electric field is given by [7]

$$E = E(t)\cos(2\pi\nu_0 t), \tag{5.2}$$

where $E(t)$ is the electric field at time t, and ν_0 is the angular frequency of the radiation. Rayleigh scattering happens when this induced dipole moment scatters electromagnetic radiation of frequency ν_0. The gathering of all vibrations in a crystalline material might be seen as the superposition of plane waves that spread to infinity [8]. These plane waves are usually displayed as quasi-particles called phonons. Considering a diatomic molecule oscillating with frequency, ν_{vib}, executing simple harmonic oscillations, the coordinate q_{vib} along the axis of oscillation at time, t, is given [9]:

$$q_{vib} = q_0 \cos(2\pi\nu_{vib} t) \tag{5.3}$$

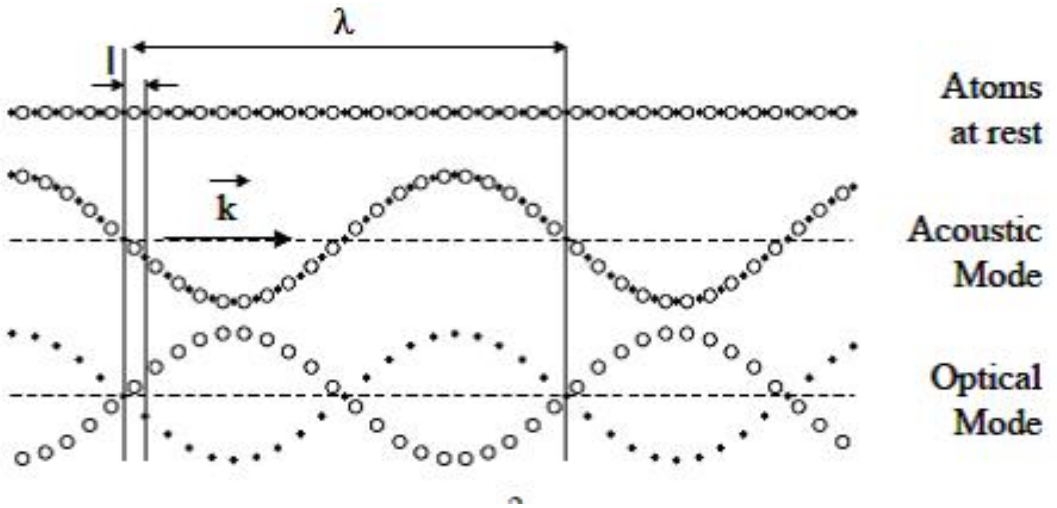

Figure 5.2: *The transverse phonons in a 1D-solid with unit cell parameter l. (Adopted from (Gouadec and Colomban, 2007)[13]).*

Eq 5.3 is a type of a normal coordinate, which is a linear combination of bond length and bond angles, and is related to all normal modes. Modes can be described as either stretching (ν), bending (δ), torsional (τ), librational (R'/T' pseudorotations/translational) or lattice modes (the last incorporate the relative displacement of the unit cells), all these rely upon the prevailing term in the normal coordinate [10]. $(3pN-6)$ diverse phonons can propagate [12] for a three-dimensional (3D) solid containing N unit cells with p atoms each and their wavevectors ($\mathbf{k}$) all point in a volume of the reciprocal space called the Brillouin Zone (BZ). There are two sorts of modes, those with in-phase vibrations of neighbouring particles and those out-of-phase vibrations. The former with lower energies are called acoustic vibrations and the latter with higher energies are called optic vibrations. Phonons can either vibrate in the direction towards the propagation of the radiation, and these are called longitudinal modes, or they can vibrate orthogonal to the direction of the radiation and called transverse modes [13].

The alteration in the dipole moment and thus polarizability throughout the oscillation will give the following Taylor approximation of the polarisability tensor ($\bar{\alpha}$) for very small amplitude [10]:

$$\alpha = \alpha^0 + \left(\frac{\partial \alpha}{\partial q_{vib}}\right)_{q_{vib}=0} \times q_{vib} \tag{5.4}$$

Combination of Eq 5.3 and Eq 5.4 becomes:

$$\alpha = \alpha^0 + \left(\frac{\partial \alpha}{\partial q_{vib}}\right)_{q_{vib}=0} q_0 \cos(2\pi\nu_{vib}t) \tag{5.5}$$

If the molecule is excited by the incoming monochromatic light of frequency ν_0, then the resulting dipole moment is given by combining Eq 5.1 and 5.2 as:

$$\mu = \bar{\alpha}E(0)\cos\left(2\pi\nu_0 t\right) \tag{5.6}$$

and substituting Eq 5.5 into Eq 5.6 the dipole moment becomes:

$$\mu = \alpha^0 E(0)\cos(2\pi\nu_0 t) + \left(\frac{\partial \alpha}{\partial q_{vib}}\right)_0 E(0)q_0 \cos(2\pi\nu_{vib}t)\cos(2\pi\nu_0 t) \tag{5.7}$$

Which can also be written as :

$$\begin{aligned} \mu &= \alpha^0 E(0)\cos(2\pi\nu_0 t) \\ &+ \left(\frac{\partial \alpha}{\partial q_{vib}}\right)_0 \frac{E(0)q_0}{2}\left[\cos\left(2\pi(\nu_0 - \nu_{vib})t\right) + \cos\left(2\pi(\nu_0 + \nu_{vib})t\right)\right] \end{aligned} \tag{5.8}$$

where the scattered electric field is proportional to μ, Eq 5.8 predicts both quasi-elastic ($\nu = \nu_0$) and inelastic ($\nu = \nu_0 + \nu_{vib}$) light scattering. The first is known as the Rayleigh scattering and the latter, which happens only when vibrations change the polarizability $\left(\frac{\partial \alpha}{\partial q_{vib}} \neq 0\right)$, is the Raman scattering.

5.1.1.2 Quantum theory of Raman effect

The theory looks at the vibrational energy of molecules as quantized energy states. As it has been mentioned before, monochromatic light can either be absorbed, scattered or go through a material when it interacts with it. In Rayleigh scattering, most of the photons from the light interacting with the material are scattered without changing the energy. In this process, the electric field of the incoming monochromatic light is in resonance with the oscillation of electrons of the material which it interacts with. Still, parallel to the afore-mentioned process, is the Raman scattering (Raman Effect) where a minuscule bulk of the incoming photons are scattered with a change in the energy. This change in photon's energy is due to mate-

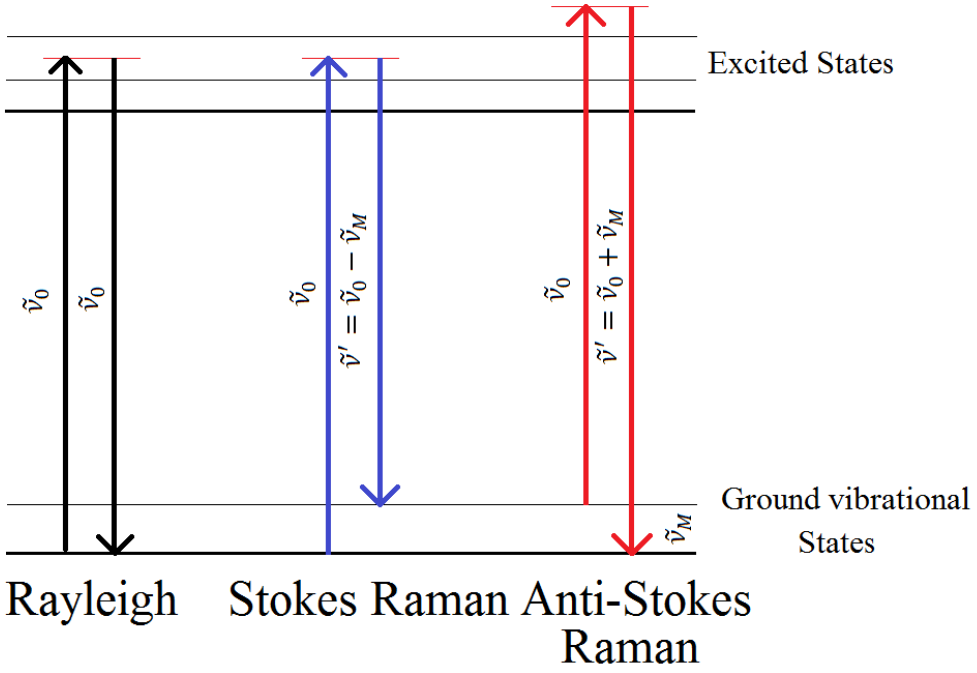

Figure 5.3: *Energy level diagram of Raman scattering that arise from a monochromatic laser incident beam on a specimen . (Adopted from (6Kittel, 1996)[8]).*

rials vibrating at the same time the electrons oscillate in resonance with the electric field of the incoming beam. The dipole moment induced by incoming light's electric field is due to vibrational modes that result in the change of the incoming photon energy. Raman shift is as a result of the difference between incoming photon energy and inelastically scattered photon energy. Figure 5.3 is the representation of Raman and Rayleigh scattering energy diagram.

The vibrations (for a simple harmonic oscillator) of the scattering can be labeled as energy, E_{vib}. The incoming light photons with energy E, frequency ν, wavenumber k, and wavelength λ, have the following relationship of the quantities.

$$E_{vib} = h\nu(v + \frac{1}{2}) \tag{5.9}$$

where v is the vibrational quantum number that can take values 0,1,2,3,... etc. Since the scattering induces a change in energy, if the frequency of the incoming photons is the same as the scattered photons ($\nu_0 = \nu_M$), then the molecule does not lose energy. However, if the

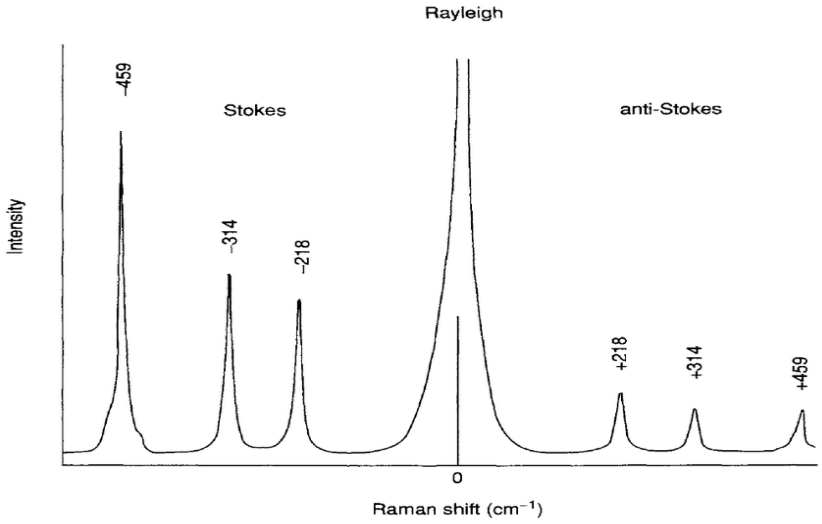

Figure 5.4: *Spectra showing the Raman Stokes, Rayleigh and Raman anti-Stokes scattering from carbon tetrachloride (CCl_4)(Adopted from (Ferraro, Nakamoto, and Brown, 2003)[15]).*

molecules of the material are excited to a higher energy than the incoming photons the photons will be scattered with frequency $\nu_0 - \nu_M$, and is called the Raman Stokes scattering. If the molecules of the material are excited to a lower energy than the incoming photons, the photons will be scattered with frequency $\nu_0 + \nu_M$ and this is called the Raman anti-Stokes scattering, as shown in figure 5.3. The Raman Stokes is the most intense of the two Raman scattering, and is the one measured in modern vibrational spectroscopy [11]. The intensity difference is due to the Boltzmann distribution, that is, the population of energy states at thermal equilibrium. Suppose there are a number of molecules N_a and N_n in the ground a and excited states n, and they have energy E_a and E_n, respectively. From Boltzmann distribution law, at thermal equilibrium the ratio of the two, will be [14]:

$$\frac{N_n}{N_a} = \frac{g_n}{g_a} \exp^{-\left(\frac{E_n - E_a}{k_B T}\right)}, \tag{5.10}$$

where g_a and g_n are degeneracies of states a and n, respectively. There are more molecules at ground state N_a than excited state N_n at room temperature. When $E_n - E_a > k_B T$, the incoming light photons have a greater chance of interacting with the molecules in the ground state

5.1.1.3 Selection rules

In quantum mechanics an oscillation is Raman-active if and when the polarizability of a molecule is altered due to the excitation or oscillation of the molecule [16]. The alteration is related to the derivative of the polarizability given by:

$$\frac{\partial \alpha}{\partial q_{vib}} \neq 0 \tag{5.11}$$

According to group theory, if a molecule is symmetric, Raman-active oscillations will not be visible in the infrared and *vice versa*. The resulting scattered intensity is directly dependent on the square of the polarizability derivative. If the incoming electric field does not alter the polarizability of the electron cloud, then the derivative of the polarizability will be close to zero, and the resulting intensity will thus be less. The extremely polar diatomic molecules such as O-H, have very weak oscillations. The dipole moment of these molecules cannot be changed by the induced oscillation of the incoming photons nor can the bending or stretching of the bonds. Some vibrational frequencies, especially in organic molecules, can be related to certain molecular excitations. Some of such cases are shown in table 5.1:

Table 5.1: Typical features of Raman spectra and their origin (Adopted from (Frost, 2006) [17]

Frequency (cm^{-1})	**Band Assignment**	**Remarks**
$2700 - 3100$	$C - H$ alkyl free vibration	Medium intensity in Raman
2230	C $\equiv$ N Stretch	Very strong band in Raman, found in most cyanide based compounds
$2190 - 2300$	C $\equiv$ C (Triple bond stretch)	Very strong in Raman
$2100 - 2140$	C $\equiv$ C (Triple bond stretch)	Very strong in Raman
$1650 - 1750$	$C = O$ Stretch	Ketones appear on the lower wavelength side, aldehydes appear on the higher side
$1600 - 1675$	$C = C$ Stretch	Very strong in Raman
$1580 - 1620$	$C = C$ Stretch	Very strong in Raman
$990 - 1010$	Aromatic ring breathing	Appears at 992 cm^{-1} for benzene, around $1004cm^{-1}$ for toluene
$650 - 850$	$C - Cl$ Stretch	Strong in Raman

5.2 Rutherford Backscattering Spectrometry

Rutherford backscattering spectrometry is a non-destructive ion beam analytical technique. It is based on the detection of energetic ions backscattered from a material of interest. It is used for near-surface analysis of thin films, identification of elemental composition of solid materials and depth profiling of individual elements [15]. In this study it was used to monitor the depth profile of the implanted Eu ions in ZrN.

5.2.1 Kinematics

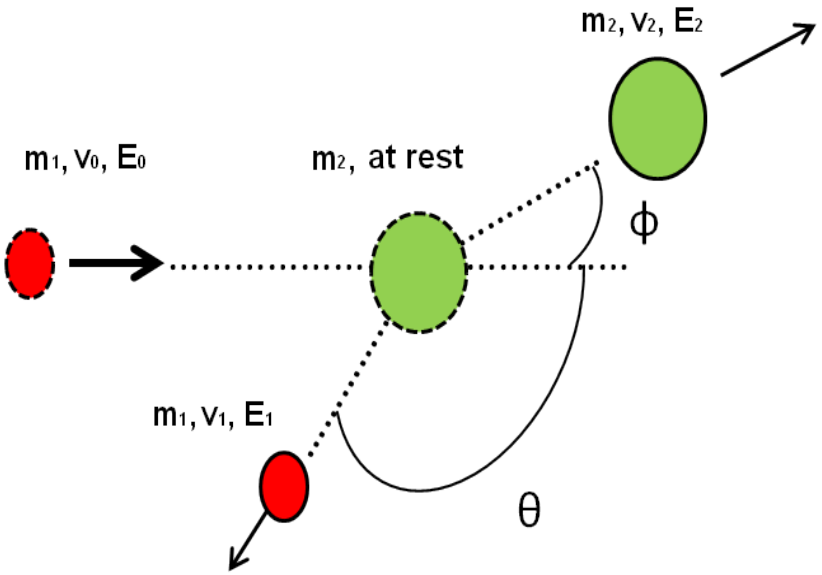

Figure 5.5: *A schematic of the scattering geometry, with recoil angle ϕ and scattering angle θ.*

In figure 5.5, the incident ion of energy E_0 and mass m_1 will interact with the atoms of the target with mass m_2. The target atoms will recoil at an angle ϕ and velocity v_2, while the incident ion is back-scattered at an angle θ with an energy E_1 less than the incident energy. Because some of the energy of the incident ion will be transferred to the target atoms causing the target atoms to recoil, energy must be conserved and the total energy will be given by,

$$E_0 = E_1 + E_2 = \frac{1}{2}m_1{v_0}^2 = \frac{1}{2}m_1{v_1}^2 + \frac{1}{2}m_2{v_2}^2 \tag{5.12}$$

also total momentum must be conserved, and it is given by,

$$P_0 = P_1 + P_2 = \begin{cases} m_1 v_0 = m_1 v_1 \cos\theta + m_2 v_2 \cos\phi & P_x \\ 0 = m_1 v_1 \sin\theta - m_2 v_2 \sin\phi & P_y \end{cases} \tag{5.13}$$

After the interaction with the surface the incident ion will scatter and result in a backscattered ion of energy E_1 given by,

$$E_1 = KE_0 \tag{5.14}$$

where K is the kinematic factor given by combining eq. 5.12 and 5.13, resulting in,

$$K = \frac{E_1}{E_0} = \left\{ \frac{m_1 \cos\theta \pm ({m_2}^2 - {m_1}^2 \sin^2\theta)^{1/2}}{m_1 + m_2} \right\}^2 \tag{5.15}$$

If the backscattering angle is constant, then K relies on the ratio m_1/m_2. When $m_1 < m_2$ then only the plus sign applies in eq. 5.15, while there are two solutions if $m_1 > m_2$, with the maximum scattering angle given by.

$$\theta_{max} = \arcsin\left(\frac{m_2}{m_1}\right) \tag{5.16}$$

If the incident beam interacts with a target that has a mass difference of Δm_2, then the backscattered beam will have a separation energy ΔE_1 from the two masses given by,

$$\Delta E_1 = E_0 \frac{dK}{dm_2} \Delta m_2 \tag{5.17}$$

Light target elements result in the ideal energy separation and mass resolution where the derivative $\frac{dK}{dm_2}$ is steep, while heavy elements result in smaller mass resolution. Using higher incident energy, E_0, or heavier incident elements, m_1, can boost the mass resolution of heavier target elements. Generally, the ideal mass resolution is achieved with incident beam of mass m_1 in the range $4 - 7$ [18].

5.2.2 Depth profile

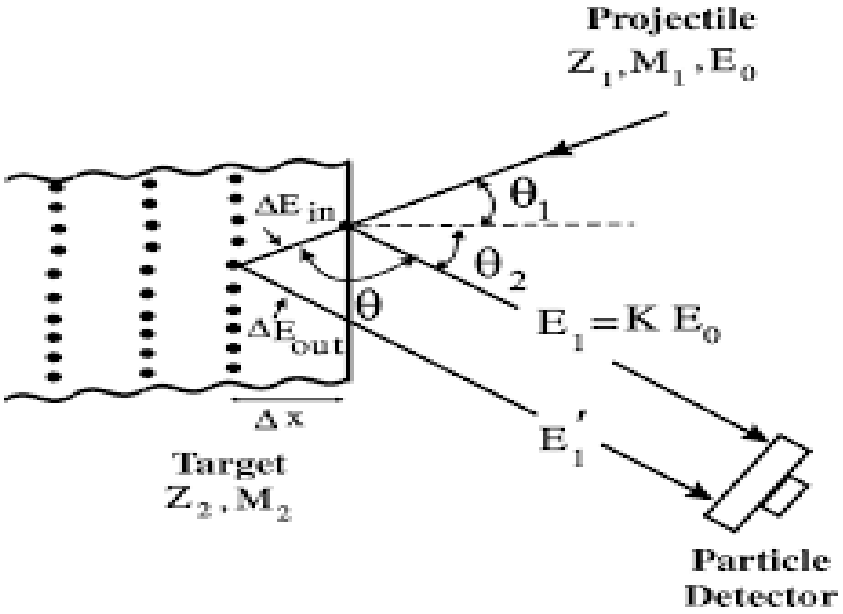

Figure 5.6: *A schematic of different scattering events in a material of bulk mass, M_2 and a projectile of mass M_1 with the beam scattered at different angles θ_1 and θ_2 [20].*

Figure 5.6 is a diagram showing the backscattering of the projectile at the surface and at a depth Δx. The projectile, α-particles, lose energy as they go into the target and hence will be back-scattered at different energies. The scattered α-particles at the surface have an initial energy E_0 and a backscattered energy of E_1 which has been defined as KE_0 in section 5.2.1 above. The α-particles backscattered at any depth Δx from the surface have an initial energy loss,$\Delta E(in)$ lower than E_0 and they are backscattered within the depth Δx at an energy loss out $\Delta E(out)$ and from the surface with energy E_1' lower than $\Delta E(out)$.

The depth where the incoming α-particles are backscattered in the target material is given by $\frac{\Delta x}{\cos\theta_1}$ (figure 5.6). However, these α-particles continue to lose energy at a depth of $\frac{\Delta x}{\cos\theta_2}$ as they exit the target. The α-particles backscattered at a depth of Δx are assumed to lose energy constantly going in and exiting the target at a rate of $\frac{dE}{dx}$ [21, 22].

The difference between the energy of the backscattered α-particles at the surface and those

exiting the surface from a depth Δx is given by

$$KE_0 - E_1' = \frac{K\Delta x}{\cos\theta_1}\frac{dE(in)}{dx} + \frac{\Delta x}{\cos\theta_2}\frac{dE(out)}{dx} \tag{5.18}$$

The energy loss factor [S], derived from eq. 5.18 can be written as

$$[S] = \frac{K}{\cos\theta_1}\frac{dE(in)}{dx} + \frac{1}{\cos\theta_2}\frac{dE(out)}{dx} \tag{5.19}$$

which gives the information about the relationship between energy and depth. Therefore, if $KE_0 - E_1'$ is taken as ΔE_1, that is

$$\Delta E_1 = KE_0 - E_1' \tag{5.20}$$

Then the relationship between [S] and ΔE_1 can be given as

$$\Delta E_1 = [S]x \tag{5.21}$$

This is comparable to eq. 5.17. If δE is the energy width and δx the depth resolution, the energy loss factor can be related to these factors by giving the depth resolution as

$$\delta x = \frac{\delta E}{[S]} \tag{5.22}$$

Therefore, this can be used to measure the depth of the implanted ions by converting the backscattered spectrum of counts as a function of energy to a spectrum of counts as a function of depth.

5.3 Scanning Electron Microscopy

Scanning electron microscopy (SEM) is a surface analysis technique that uses electrons instead of light. When electrons interact with the specimen's surface, various secondary excitations result at different depths from the surface as shown in figure 5.7 (b). Equations 5.23 and 5.24 show the interaction depth (z) and the width (x) given in units μm, these are parameters for the impinging electrons which are directly proportional to the accelerating voltage, E_0 in keV

and the density of the target material, ρ in g/cm^3 [23].

$$z = \left(\frac{0.1{E_0}^{1.5}}{\rho}\right) \tag{5.23}$$

$$x = \left(\frac{0.077{E_0}^{1.5}}{\rho}\right) \tag{5.24}$$

The modern scanning electron microscope is equipped with three principal analytical techniques, which are the secondary electron (SE) detection, backscattered electron (BSE) detection and energy dispersive spectroscopy (EDS) - X-ray detection. The secondary electrons are inelastically scattered from the specimen surface, they have low energy which makes for perfectly imaging topographic features.

A system of magnetic lenses is used to focus an electron beam to a spot of around 1-10 nm diameter. Elastic and inelastic scattering results when the incident electrons interact and impinge the surface of the target. This results in the impinging electrons exiting after traveling through the sample. The material volume where the impinging electrons are backscattered is bigger compared to that of the secondary electrons, therefore the lateral resolution is smaller.

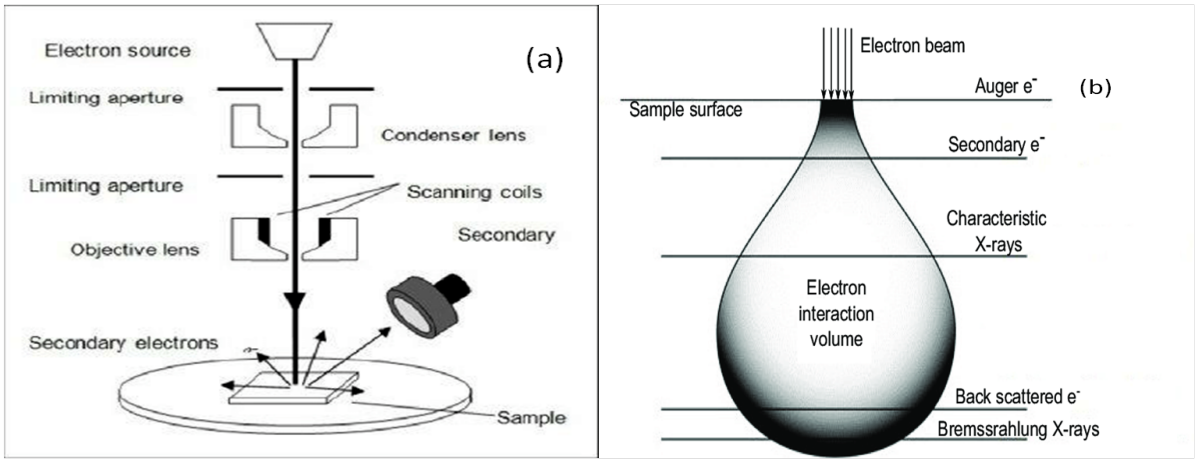

Figure 5.7: *(a) Schematic diagram of a scanning electron microscope [24] and (b) a schematic of the electron cascade that spreads out into an interaction volume [25]*

The number of backscattered electrons produced is dependent on the atomic number of the target sample. Therefore, a brighter image will be produced from a target sample with higher

atomic number. The detector used in the scanning electron microscope can either be the less effective metals or the most effective scintillator/light pipe/photomultiplier [26]. The current of the impinging electrons is about 10^{-8} to 10^{-7} A.

There are two types of materials that can be characterized with scanning electron microscopy; conducting and non-conducting materials. In conducting materials, the impinging electrons are conducted away from the point of incidence while in non-conducting materials, the impinging electrons will be concentrated at the point of incidence causing a charging of the surface. The result will be an electrostatically charged surface which will deflect the incoming electrons leading to a distorted image. To reduce this effect in non-conducting materials, a conducting layer with a thickness of around 5-10 nm is sputtered onto the surface of the non-conducting material. This will allow conduction of excess electrons which will lower the charging effect. This however, can result in a reduction in the resolving power of the SEM, because the surface of the sample will be covered making it difficult to gain any topographical information from the sputtered layer [27].

The resolution of SEM as mentioned above is determined by the charging effect of the non-conductive material surface. However, the other factor that determines the resolution is the electron beam width. High resolution will result from narrow(er) electron beams [28]. Therefore, equation 5.25 gives broadening (${d_p}^2$) of the spot size, d_p as a function of the accelerating voltage:

$$ {d_p}^2 = \frac{1}{\alpha}^2 \left[\frac{i}{B} + \lambda^2 \right] + \left[\frac{\Delta E}{E_0} C_c \right]^2 \alpha^2 + \left[\frac{1}{2} C_s \right]^2 \alpha^6 \tag{5.25} $$

where it is given by the sum of broadening effects, where the first contributor is the beam, given by the properties: α the divergence angle of the beam, B the brightness of the source and i the beam current. The second contributor to the broadening of the spot size is given by the diffraction of the electrons of wavelength λ given by the size of the final aperture. The third and fourth contributors are due to the broadening caused by the chromatic and spherical aberrations, respectively. If all contributions are as small as possible, the smallest spot size can be obtained. A decrease in the accelerating voltage will result in the decrease in the electrons

wavelength and an increase in the chromatic aberration. This will result in the increase in the spot size and therefore a decrease in the SEM resolution [29].

The field emission gun (FEG) has high brightness, and this will make the first contributor in equation 5.25 small as possible. This will result in a small energy spread, ΔE in the electron energies. This together with the fact that the chromatic and spherical coefficients C_c and C_s, respectively, can be reduced by optimizing the lenses for low-energy electrons, providing the FEG low voltage SEM with high resolving power.

5.4 X-ray diffraction

If one considers the orientation and interplanar spacing of parallel planes inside the crystal and characterize them by three integer numbers h,k,l called indices, a mathematical model can be employed that utilizes three dimensional diffraction gratings and the three indices become the order of diffraction along the unit cell axes a, b, and c, respectively. In the event that is considered on figure 5.8 where an approaching X-ray beam is hitting two parallel planes, isolated by an interplanar spacing d, the parallel approaching beams A and A' make an angle θ with these planes.

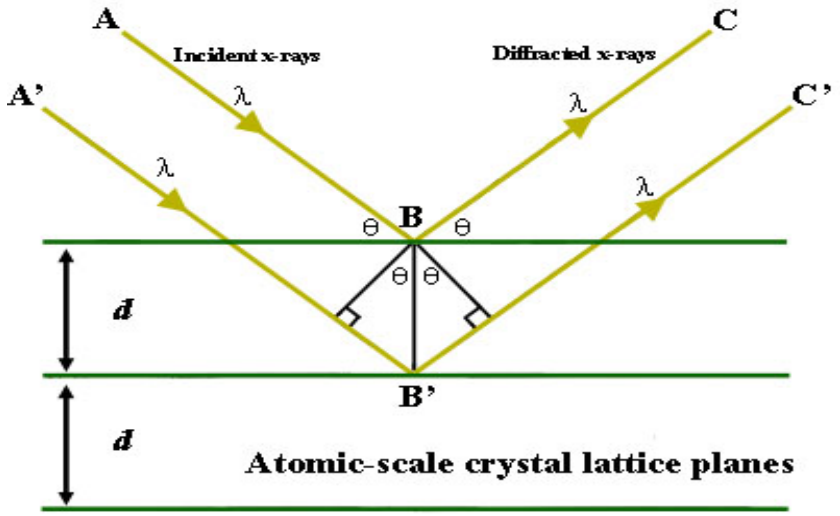

Figure 5.8: *Bragg's Law of reflection. The diffracted X-rays exhibit constructive interference when the distance between paths ABC and A'B'C' differs by an integer number of wavelengths(λ)[30]*

On the off chance that the waves represented by C and C' in figure 5.8 are in phase, the diffracted beam of maximum intensity will come about. The distinction in path length between A to C and A' to C' is the integral number of wavelengths, λ. The mathematical relationship is known as Bragg's law, which is given by

$$2d \sin\theta = n\lambda \tag{5.26}$$

The process of diffraction is portrayed in terms of the incoming and diffracted beams, each making an angle θ with the fixed crystal plane. Diffraction happens from planes set at the angle θ regarding the incoming beam and creates a diffracted beam at an angle 2θ from the incoming beam.

Conceivable d-spacing given by the three indices h,k,l are portrayed by the shape of the unit cell. Re-arranging Bragg's law the result is:

$$sin\theta = \frac{\lambda}{2d} \tag{5.27}$$

Consequently, the unit cell dimensions describe the conceivable 2θ values where there can be diffraction. In any case, the intensities of the diffraction are dictated by the appropriation of

the electrons in the unit cell. We locate the highest electron density around the atom. In this way, the intensities depend on what sort of atoms we have and where in the unit cell they are found. Planes experiencing regions with high electron densities will diffract strongly, planes with low electron density will give weak intensities [31].

5.4.1 Bragg-Brentano (θ-2θ) mode

Most XRD patterns are generated using the measurement setup of the Bragg-Brentano geometry [32], shown in figure 5.9 (a). In this configuration θ is the incidence angle of the incident X-rays measured with respect to the surface of the sample, and 2θ is the diffracted angle. In the Bragg-Brentano geometry, the setup is such that the X-ray source and the detector are placed so that the incidence angle and the diffracted angle remain the same throughout the scanning measurements. This therefore, results in only the crystal planes parallel to sample surface being probed.

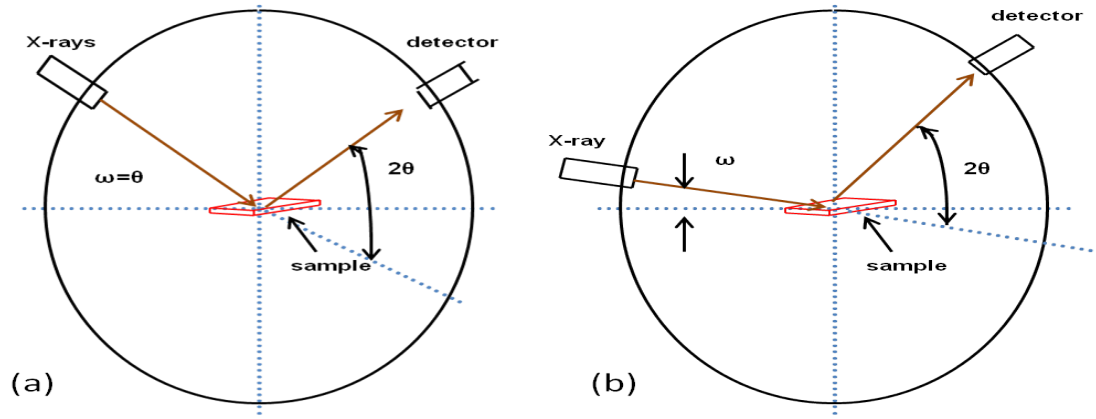

Figure 5.9: *(a) Schematic diagram showing the Bragg-Brentano (θ-2θ) and (b) the grazing incidence XRD geometry*

5.4.2 Grazing incidence X-ray diffraction(GIXRD) mode

In the Bragg-Brentano mode, the X-ray penetration depth is large and the spectrum is given by diffractions from close to the substrate. Grazing incidence X-ray diffraction is used to lessen this problem. In the GIXRD setup, X-rays penetrate the specimen at small fixed incidence

angles and hence increasing the X-ray traveling path in the specimen as shown in figure 5.9 (b). Therefore, the detector is varied to obtain the spectra since the incidence angle is fixed, and this assist in investigating different crystal orientations in the specimen.

Bibliography

[1] Jiao, L., Yu, K.Y., Chen, D., Jacob, C., Shao, L., Zhang, X. and Wang, H., (2015). 'Radiation tolerant nanocrystalline ZrN films under high dose heavy-ion irradiation'. *Journal of Applied Physics*, 117(14), p.145901.

[2] Raman, C. V. and Krishnan, K. S., (1928). 'A new class of spectra due to secondary radiation'. *Indian Journal of Physics*. Vol. 419, pp. 399 - 419

[3] Garfield.library.upenn.edu. (2020). [online] Available at: `http://garfield.library.upenn.edu/classics1983/A1983QT44500001.pdf` [Accessed 23 Jan. 2020].

[4] Stavola, M., (2001). Semiconductors, Local Vibrational Mode Spectroscopy of.

[5] Curtis, K., Dorney, J., Esmonde-White, K., Fullwood, N. J., Gardner, B., Martin-Hirsch, P. L., Walsh, M. J., McAinsh, M. R., Stone, N. and Martin, F. L., (2016). 'Using Raman spectroscopy to characterize biological materials'. *Nature Protocols*. Vol. 6, pp. 664-687

[6] Kauffmann, T.H., Kokanyan, N. and Fontana, M.D., (2019). 'Use of Stokes and anti-Stokes Raman scattering for new applications'. *Journal of Raman Spectroscopy*, 50(3), pp.418-424.

[7] Bruno, G., (2002). 'Classical theory of rayleigh and raman scattering'. *The Raman Effect: A Unified Treatment of the Theory of Raman Scattering by Molecules*, pp.31-48.

[8] Kittel, C., McEuen, P. and McEuen, P., (1996). 'Introduction to solid state physics'(Vol. 8, pp. 105-130). New York: Wiley..

[9] Vandenabeele, P., (2013). 'Practical Raman spectroscopy: an introduction'. *John Wiley & Sons*.

[10] Prinsloo, L.C., (2009). 'Micro-Raman spectroscopy of nanomaterials: applications in Archaeology'(Doctoral dissertation, University of Pretoria).

[11] Hassing, S., (2019). 'What Is Vibrational Raman Spectroscopy: A Vibrational or an Electronic Spectroscopic Technique or Both?'. *In Modern Spectroscopic Techniques and Applications*. IntechOpen.

[12] Colomban, P., (1989). 'Gel technology in ceramics, glass-ceramics and ceramic-ceramic composites'. *Ceramics International*. 15(1), pp. 23-50

[13] Gouadec, G. and Colomban, P., (2007). 'Raman Spectroscopy of nanomaterials: How spectra relate to disorder, particle size and mechanical properties'. *Progress in Crystal Growth and Characterization of Materials*. 53(1), pp. 1-56

[14] Ott, J.B. and Boerio-Goates, J., (2000). *Chemical Thermodynamics: Advanced Applications: Advanced Applications*. Elsevier.

[15] Ferraro, J. R., Nakamoto, K., Brown, C. W., (2003). *Introductory Raman Spectroscopy*. 2nd edn, Elsevier Ltd.

[16] Ferraro, J.R., (2003). *Introductory raman spectroscopy*. Elsevier.

[17] Frost, R. L., (2006). 'A Raman spectroscopic study of selected minerals of the rosasite group'. *Journal of Raman Spectroscopy*. 37(9), pp. 910-921

[15]Han, B., Wang, Z., Devi, N., Kondamareddy, K.K., Wang, Z., Li, N., Zuo, W., Fu, D. and Liu, C., (2017). 'RBS depth profiling analysis of (Ti, Al) N/MoN and CrN/MoN multilayers'. *Nanoscale research letters*, 12(1), pp.1-8.

[18] Mayer, M., (2003). 'Rutherford backscattering spectrometry (RBS)'. *In Workshop on Nuclear Data for Science and Technology: Materials Analysis* (Vol. 34).

[19] Micelotta E.R., Jones A.P., and Tielens A.G.G.M., (2010)Astronomy and Astrophysics A 36

[20] Verma, H.R., (2007). 'Atomic and nuclear analytical methods'. Springer-Verlag Berlin Heidelberg.

[21] Chu, W.K., Mayer, J.W. and Nicolet, M.A., (1978). Backscattering Spectrometry Academic Press. New york.

[22] Tesmer, J.R. and Nastasi, M., (1995). 'Handbook of modern ion beam materials analysis'. Materials Research Society, 9800 McKnight Rd, Suite 327, Pittsburgh, PA 15237, USA, 1995. 700.

[23] Potts, P.J. and Cresser, M., (1987). 'A handbook of silicate rock analysis'. *Analytica Chimica Acta*, 201, pp.363-363.

[24] Mukhopadhyay, A., (2015). 'Measurement of magnetic hysteresis loops in continuous and patterned ferromagnetic nanostructures by static magneto-optical kerr effect magnetometer'. Guwahati: Satyendra Nath Bose National Centre for Basic Sciences.

[25] Marturi, N., (2013). 'Vison and visual servoing for nanomanipulation and nanocharacterization using scanning electron microscope'. (Doctoral dissertation, Besançon).

[26] Zhou, W., Apkarian, R., Wang, Z.L. and Joy, D., (2006). 'Fundamentals of scanning electron microscopy (SEM)'. *In Scanning microscopy for nanotechnology* (pp. 1-40). Springer, New York, NY.

[27] Goldstein, J.I., Newbury, D.E., Echlin, P., Joy, D.C., Romig, A.D., Lyman, C.E., Fiori, C. and Lifshin, E., (1992). 'Coating and conductivity techniques for SEM and microanalysis'. *In Scanning Electron Microscopy and X-Ray Microanalysis* (pp. 671-740). Springer, Boston, MA.

[28] Brabazon, D., and Raffer, A., (2010). 'Advanced characterization techniques for nanostructures'. *In Emerging nanotechnologies for manufacturing*, pp. 59-91. William Andrew Publishing.

[29] Hafner, B., (2007). 'Scanning electron microscopy primer'. *Characterization Facility, University of Minnesota-Twin Cities*, pp.1-29.

[30] Henry, D., Eby, N., Goodge, J., Mogk, D., (2016). 'Geochemical Instrumentation and Analysis: X-ray reflection in accordance with Bragg's Law'. *Carleton College: Integrating Research and Education*. Accessed 26 August 2019, `https://serc.carleton.edu/research_education/geochemsheets/BraggsLaw.html`

[31] Lei.lt. (2020). [online] Available at: `http://www.lei.lt/_img/_up/File/atvir/renginiai/XRDanalysis.pdf` [Accessed 31 Jan. 2020].

[32] Widjonarko, N.E., (2016). 'Introduction to advanced x-ray diffraction techniques for polymeric thin films'. *Coatings*, 6(4), p.54.

Chapter 6

Experimental Procedure

The radiation tolerance of ZrN and the migration behaviour of implanted Eu in ZrN were investigated using Raman spectroscopy, RBS, SEM and GIXRD. The structural changes due to swift Xe ions and migration behaviour of Eu were investigated for annealed samples at 800 and 900 ^{o}C for 5h. This chapter presents the sample preparation, the irradiation conditions, thermal annealing at 800 and 900 ^{o}C and the analysis of both the as-deposited and irradiated ZrN samples.

6.1 Sample Preparation

The ZrN layers of about 20 μm thickness were fabricated using the vacuun arc-vapour deposition at the Belarusian State University in Minsk, Belarus. The process entails the condensation of a material in vacuum facilitated by ion bombardment onto a silicon substrate. Before the ZrN layers could be deposited, the surface of the silicon substrate was etched by Zr ion bombardment for 1 minute with the bias at -1 kV. The arc current of 100 A for the Zr cathode was used in the vacuum chamber kept at 10^{-3} Pa. This results in the cleaning and heating of the substrate to temperatures between 450 and 5000 ^{o}C. The deposition of the ZrN layers is then instigated by introducing the N_2 gas into the chamber at a pressure of 0.1 Pa using a substrate bias of -120 V. The continuous bombardment with zirconium ions on the growing coating ensures a nanocrystalline structure. The zirconium ions are accelerated by a negative substrate bias voltage. To achieve a thickness of 20 μm, the deposition is simultaneously done using two Zr cathodes for approximately 40 min.

6.2 Irradiation

Low-energy Xe implantation was done at the Facility for Modification and Analysis of Materials with Ion Beams (FAMA) at the Vinča Institute of Nuclear Sciences, Belgrade, Serbia. The implantation was performed at room temperature using 360 keV Xe ions at an ion fluence of $1.1 \times 10^{16} cm^{-2}$.

The high-energy irradiation with the Xe ions was done at the U-400 and IC-100 cyclotrons at the Flerov Laboratory on Nuclear Reactions (FLNR), Joint Institute for Nuclear Research (JINR), Dubna, Russia. During irradiation, the ion beam homogeneity of greater than 5% is maintained at the surface of the deposited layer. The target temperature was kept at 30^{o}C during irradiation. The specimen were irradiated with 167 MeV Xe ions at an ion fluence of $6.77 \times 10^{14} cm^{-2}$.

The low-energy implantation of the Eu ions was performed at the Friedrich-Schiller University in Jena Germany. The implantation was performed at room temperature using 360 keV Eu ions at fluence $1.0 \times 10^{16} cm^{-2}$.

6.3 Thermal Annealing

In this study, as-deposited, ion implanted and irradiated ZrN layers were all thermally annealed at 800 and 900^{o}C for 5 hours each and then analyzed. Thermal annealing of irradiated layers is important because it helps study the migration of implanted ions in the material for application in nuclear environments, for instance [1]. It also helps with structural alterations and alteration in physical and chemical properties for certain applications.

The annealing was done using a computer controlled *Webb 77* graphite furnace. To prevent contamination of the samples, glassy carbon crucibles are used to hold the samples. The sample in the crucible is then put in the furnace chamber. The furnace is then closed and evacuated to

a low pressure of about 10^{-6} mbar. During annealing the pressure needs to be kept at around 10^{-3} mbar to maintain vacuum, and to ensure this, the furnace is degassed before annealing.

6.4 Sample characterization

6.4.1 Raman Spectroscopy

The Raman spectroscopy measurements in this study were carried out using the *WItec alpha RAS+* spectrometer. The acquisition of the image scans was performed using a 532 nm excitation laser with a laser power of 15 mW and a $50\times/0.75$ numeric aperture objective with a spot size of 433 nm. The cross-sectional image scans were acquired over 40×40 μm^2 area with 150 points per line and 150 lines per image using the integration time of 1s. Cross-sectional measurements were done on the swift heavy ions irradiated samples on an uneven cross-sectional surface and characterized with cluster analysis (distribution maps).

6.4.2 Rutherford backscattered spectrometry

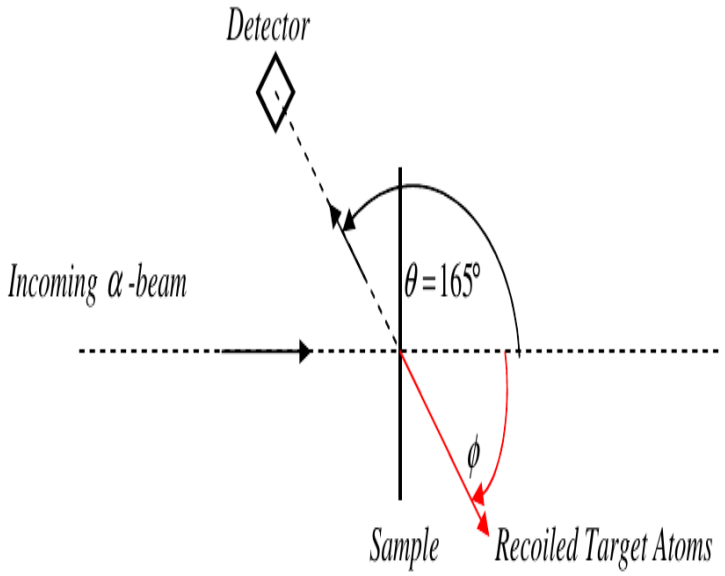

Figure 6.1: *A schematic of a scattering geometry used in this study.*

Figure 6.1 is the scattering geometry setup used in this study which has the incident beam coming in a direction normal to the plane of the sample, and the target atoms are recoiled at the angle ϕ. The detector is placed such that the beam is backscattered at an angle of 165^o with respect to the incoming beam. The setup is chosen because it allows a large scattering angle, which is good for optimizing the mass resolution, it's also good at incorporating a large range of grazing incident and exit angles, optimizing the depth resolution.

The ions are produced by an ion source and then accelerated by an ion accelerator. The RF ion source was used to produce helium ions (He^+). The He^+ ions were then accelerated by a 2.0 MeV Van de Graff accelerator at University of Pretoria. In this study He^+ ions of $1.8\,MeV$ were used. The ions are accelerated through a beam-line/tube which focuses and guides the beam of $^4He^+$ ions into the analysis chamber. The beam-line of the accelerator used is maintained at a pressure of $10^{-9}\,mbar$ to minimize collisions between the beam and residual gases. The analysis chamber is also maintained at a low pressure during analysis. Inside the chamber, the Eu implanted ZrN was mounted perpendicular to the incoming beam with silicon surface barrier detector mounted at 165^o. Secondary electrons were suppressed by applying a negative voltage of $\approx 200\,V$ in front of the target. The detector employs a reverse bias voltage $\approx 40\,V$ to detect the backscattered ions.

6.4.3 Scanning electron microscopy

The as-deposited sample was broken under liquid nitrogen. The sample's cross-section was then analyzed using the Zeiss Gemini Ultra Plus FEG scanning electron microscope equipped with backscattered (BS), energy-dispersive X-ray spectroscopy (EDS) and electron backscattered diffraction (EBSD) detectors. The field emission gun (FEG) is used to produce an image by scanning the sample with high energy beam of electrons. The in-lens detection of this system is used to effectively minimize the time-to-image, by detecting in parallel the secondary and backscattered electrons to guarantee optimal signal detection. A beam energy of 2 kV employing a 10 μm spatial resolution was used to show the different layers such as the sample holder, the deposited ZrN layer, and the Si substrate. A cursor was then used to mark-out the deposited layer and measure the width of it.

6.4.4 Grazing incidence X-ray diffraction

The grazing incidence X-ray diffraction (GIXRD) analysis was done at the South African Nuclear Energy Corporation (NECSA) using Bruker D8 Discover equipment. The analysis was done on the as-deposited ZrN. The Cu(Kα) X-ray radiation source with a wavelength of 1.5418 $\mathring{A}$ was used. The spectra were collected at a 2θ step size of 0.03^o and dwelling time of 240 s per frame (four frames). The incident X-ray beam was retained at 0.5^o relative to the surface of the sample and the diffraction pattern collected by the detector rotated by the goniometer from 22^o to 120^o 2θ. The diffraction peaks of the as-deposited ZrN were indexed to a cubic structure of stoichiometric ZrN with a space group of Fm-3m and cell parameters: $a = 4.585\mathring{A}$, $a/b = 1.0000$, $b/c = 1.0000$ and $c/a = 1.0000$ using the best matching Inorganic Crystal Structure Database (ICSD) card # 41934.

Bibliography

[1] De Broglie, I., Beck, C.E., Liu, W. and Hofmann, F., (2015). 'Temperature dependence of helium-implantation-induced lattice swelling in polycrystalline tungsten: X-ray micro-diffraction and Eigenstrain modelling'. *Scripta Materialia*, 107, pp.96-99.

Chapter 7

Results and discussion

Zirconium nitride (ZrN) layers were deposited onto silicon substrates using vacuum arc deposition. Some of the as-deposited samples were individually implanted with Xe ions of 360 keV to a fluence of 1.0×10^{16} cm^{-2} and Eu ions of 360 keV to a fluence of 1.0×10^{16} cm^{-2}. Other samples were irradiated with swift Xe ions of 167 MeV to a fluence of 6.77×10^{14} cm^{-2}. Implantations and irradiation were performed at room temperature. The implanted and irradiated samples were then annealed at 800 and 900 ^{o}C for 5h. The as-deposited, implanted, irradiated, implanted then annealed and irradiated then annealed were characterized by different techniques. This chapter presents and discusses the findings.

7.1 As-deposited

The as-deposited samples were characterized by SEM, GIXRD and Raman spectroscopy. The thickness of the ZrN films deposited onto the silicon substrate was determined using cross-sectional SEM. The cross-sectional SEM samples were prepared by breaking the as-deposited samples under liquid nitrogen. Figure 7.1 shows the cross-sectional SEM micrograph of the as-deposited sample. The as-deposited ZrN layer is indicated as ‘‘ZrN’’and the substrate as ‘‘Si’’in figure 7.1. The as-deposited ZrN layer was found to be about 20 μm.

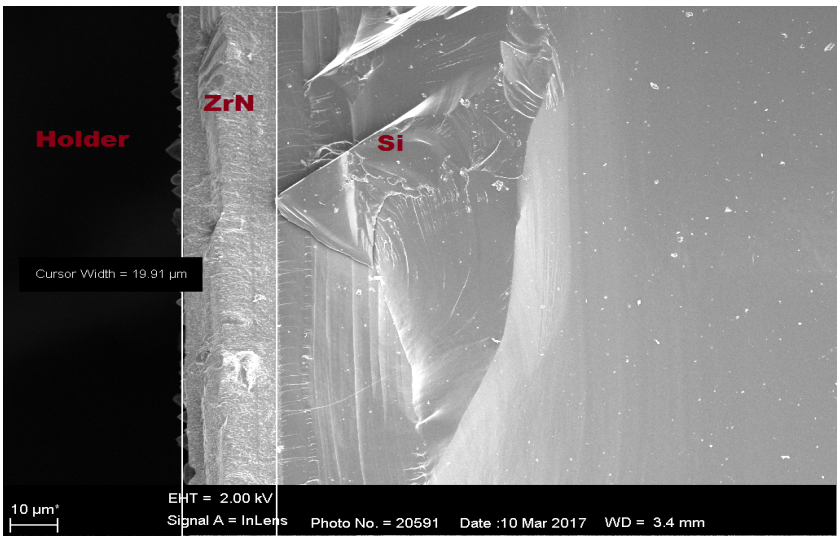

Figure 7.1: *Cross-sectional SEM-micrograph of ZrN deposited on a silicon substrate.*

Figure 7.2 shows the GIXRD pattern of the as-deposited ZrN layers. The peaks were indexed to a cubic structure of stoichiometric ZrN with a space group of $Fm\overline{3}m$ and cell parameters: $a = 4.585\mathring{A}$, $a/b = 1.0000$, $b/c = 1.0000$ and $c/a = 1.0000$ using the best matching Inorganic Crystal Structure Database (ICSD) card. The peaks at 2θ positions of 34.595^o, 40.014^o, 56.893^o, 67.958^o, 71.432^o, 83.626^o, 97.935^o and 111.228^o correspond to (111), (200), (220), (311), (222), (400), (420) and (422) ZrN planes respectively. The most preferred plane (311) was used to calculate the crystallite size using the Scherrer's equation:

$$D(nm) = \frac{K\lambda}{\beta \cos\theta_B} \tag{7.1}$$

where D is the crystallite size, K is the dimensionless shape factor (0.94), λ is the Cu(Kα) source wavelength used which is 1.5418 $\mathring{A}$, β is the full-width-half-maximum (FWHM) of the peaks in radians, and θ_B is the Bragg angle also in radians. The crystallite size was found to be 10.364 nm which makes the deposited layer a polycrystalline.

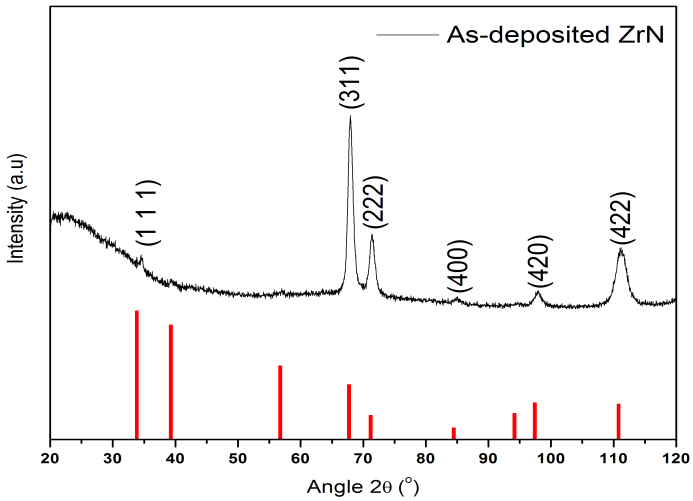

Figure 7.2: *The GIXRD pattern of the as-deposited ZrN.*

Figure 7.3 shows the Raman spectrum of the as-deposited ZrN. Defect-free ZrN has a cubic NaCl structure with every Zr and N at the site of octahedral face-centered site symmetry, hence, the first-order Raman vibrations are forbidden as has been found in similar refractory ceramics [1, 2, 3, 4, 5]. However, it is expected that physical vapour deposited layers would have inherent microscopic defects such as both heavier and lighter ion site vacancies [6]. These defects perturb the octahedral symmetry resulting in the appearance of first-order Raman vibrational modes [7]. The Raman spectrum in figure 7.3 has first-order (acoustic and optical) and second-order (acoustic) modes. The acoustic region has two acoustic modes: the transverse acoustic (TA) at 169 cm^{-1} and longitudinal acoustic (LA) at 230 cm^{-1} and optical modes: the transverse optical (TO) at 457 cm^{-1} and longitudinal optical (LO) mode at about 510 cm^{-1}. In the region 360 $-$ 410 cm^{-1} between the acoustic and optic regions is the low-frequency second-order modes 2TA at 338 cm^{-1} and TA+LA at 407 cm^{-1} labeled as 2A in figure 7.3. A considerable study of a similar refractory material TiN has assigned the acoustic region predominantly to the vibration of the heavier atoms and the optic region to the vibration of lighter nitrogen atoms [1, 2, 3, 4]. The appearance of second-order phonons according to ref [6] is an indication of the refractory material with less stoichiometric defects. In summary, the SEM, XRD and Raman spectroscopy results indicate that a 20 μm, poly-nanocrystalline ZrN films with defects was successfully deposited onto the Si substrate.

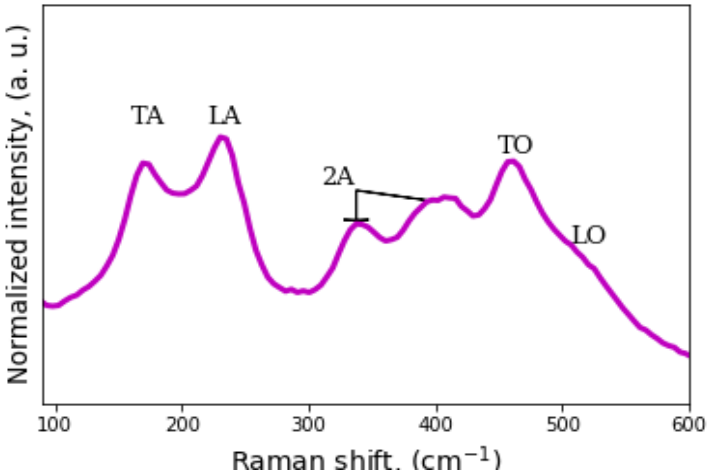

Figure 7.3: *The Raman spectrum of the as-deposited ZrN.*

7.2 Implantation and SHI Irradiation

Eu and Xe ions of energy 360 keV implanted into ZrN at a fluence of 1×10^{16} cm^{-2} and Xe ions of energy 167 MeV irradiated into ZrN at a fluence of 6.77×10^{14} cm^{-2} were simulated using SRIM2012. Figure 7.4 shows the simulation results. The simulation of Low-energy implantation of Xe, figure 7.4 (a) has a Gaussian distribution with kurtosis (K) of approximately 3 (2.27) and skewness (γ) of approximately 0 (0.26) with a projected range (Rp) of 68 nm. This implantation resulted in the maximum damage of 76 dpa at a depth of 44 nm below the surface. The electronic and nuclear energy losses at the surface were found to be 0.7 and 4 keV/nm, respectively. The simulation of Low-energy implantation of Eu, figure 7.4 (b), also has a Gaussian distribution with K $\sim$ 3 (2.76) and $\gamma \sim 0$ (0.21) with Rp of about 60 nm while maximum damage of about 80 dpa were created at a depth of 40 nm below the surface. The electronic and nuclear energy losses at the surface were found to be 0.9 and 5 keV/nm, respectively. The similarities in the nuclear and electronic energy losses on the ZrN indicate that individual implantation of Xe and Eu might result in relatively the same defect concentration, predominantly nuclear energy loss.

In figure 7.4 (c) is the swift heavy Xe ion distribution with K = 13.16 and γ = -2.15 ($\gamma < 0$, K $>$ 3) in ZrN. The maximum concentration of Xe swift heavy ions are found at a projected

range of about 9 μm below the surface. The SHI irradiation caused a maximum vacancies at a depth of about 9 μm with about 2.5 dpa. The electronic and nuclear energy loss of the swift Xe ions at the surface were found to be around 30 and 0.14 keV/nm, respectively.

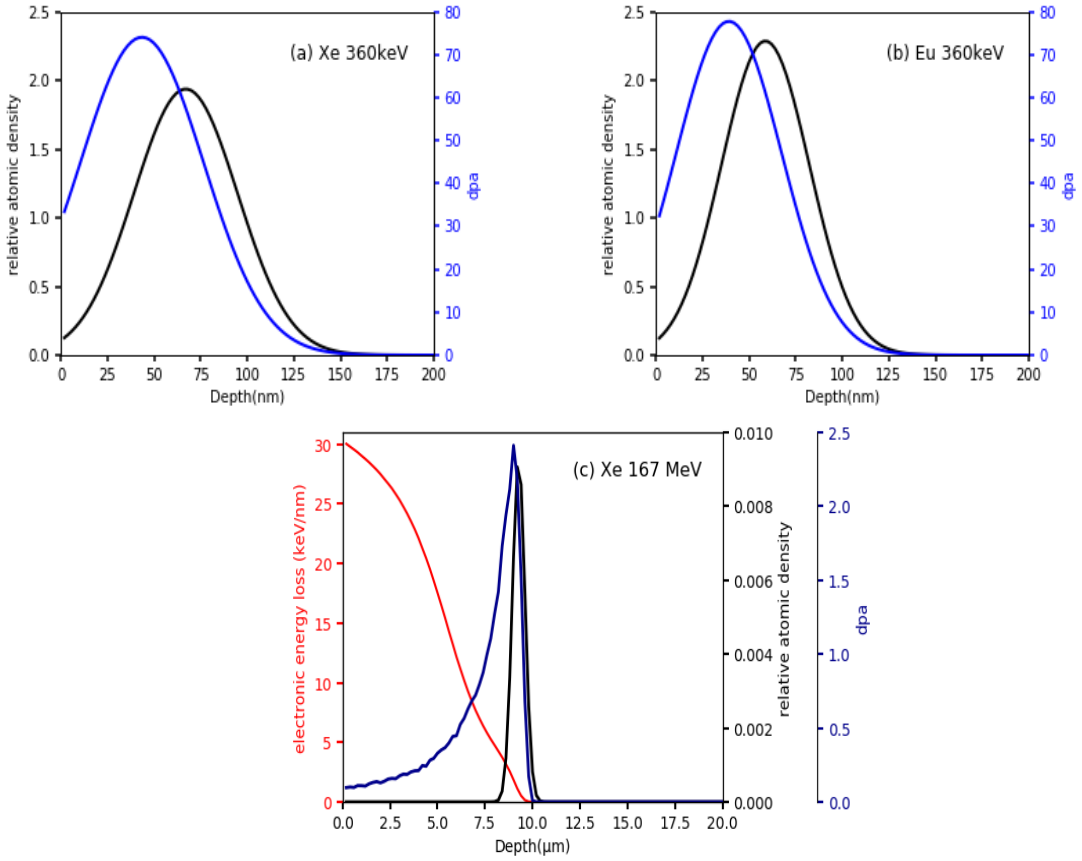

Figure 7.4: *SRIM simulated distribution profiles of relative atomic density, and displacement per atom (dpa) for (a) 360 keV Xe ions, (b) 360 keV Eu ions, with (c) the electronic energy loss of 167 MeV Xe ions irradiated into ZrN*

Figure 7.5 (a) shows the Raman spectra of Xe implanted ZrN and that of the as-deposited ZrN. Xe implantation resulted in increase in the intensity of the TA mode accompanied by the broadening of TA and LA modes while the LA intensity remained the same. Concurrently, the 2A modes broadened and completely combined. The reduction in TO intensity accompanied by broadening were also observed. These results indicate the accumulation of defects [6, 8].

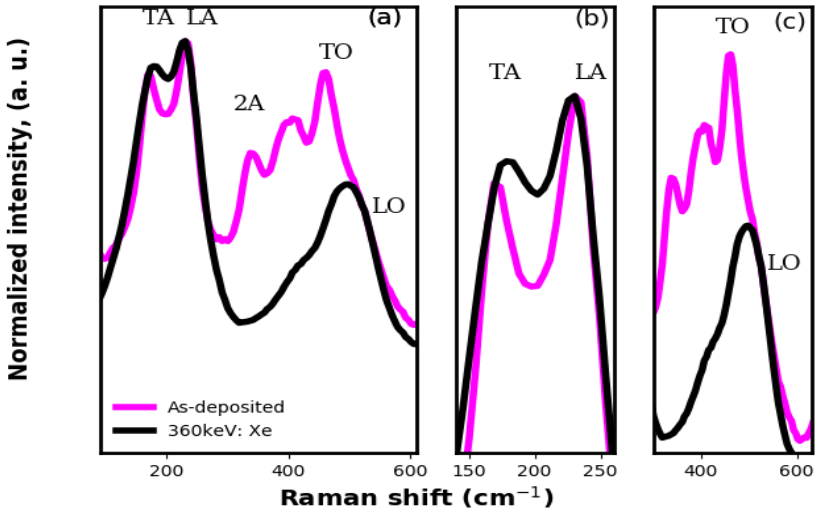

Figure 7.5: *Raman spectra of ZrN as-implanted with Xe ions with as-deposited for comparison, (b) TA and LA modes and (c) TO and LO mode of the spectra in (a)*

Raman spectra of Eu implanted ZrN and as-deposited ZrN are shown in figure 7.6. Raman results of Eu implanted ZrN are similar to Raman results of the Xe implanted ZrN, indicating equivalent concentration of defects in these implanted ZrN. This was expected as both implanted ions had relatively the same electronic and nuclear energy losses values as discussed in the SRIM simulation results. To get more insight in the radiation damage retained by these two implanted ions the Raman peak positions of the ZrN implanted spectra were compared. The summary of peak positions can be found in Table 7.1. The Xe implanted ZrN had TA at position 178 cm^{-1}, LA at 230 cm^{-1} and LO at 498 cm^{-1} while the Eu implanted ZrN had TA at 174 cm^{-1}, LA at 226 cm^{-1}, and LO at 494 cm^{-1}. These peak shifts to higher frequencies compared to the as-deposited ZrN are caused by strain in the ZrN structure after implantations as observed in silicon and SiGe [9]. The similarities in peak shifts in the two implanted ZrN indicate similar strain caused by the implanted ions, which further confirm both implantations caused similar implantation effects.

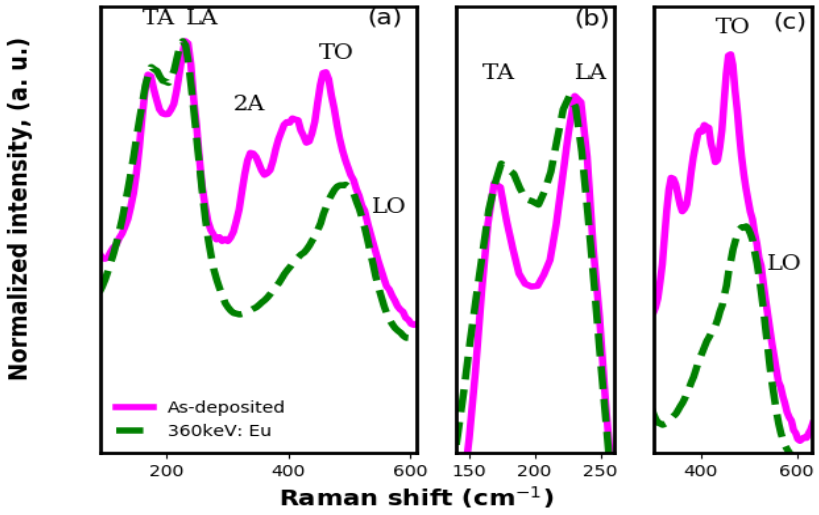

Figure 7.6: *Raman spectra of ZrN as-implanted with Eu ions with as-deposited for comparison, (b) TA and LA modes and (c) TO and LO mode of the spectra in (a)*

Figure 7.7 shows the Raman spectra of Xe irradiated ZrN and the as-deposited ZrN. The spectrum of irradiated ZrN shows all modes with a decrease in the intensity of the TA mode and the low-frequency second-order modes (2A) while the LA mode remain the same. The combination of the TO and LO modes and a subsequent decrease in the intensity was also observed. These indicates the increase in lattice disorder around the nitrogen lattice sites, the same effect was observed with doping carbon to TiN where carbon affected the optical region of TiN because of its relative size to nitrogen [6]. Similar results have been reported on ZrN irradiated with similar swift heavy ions, and were explained to be due to point defects formed through a high density electronic excitations of ZrN via the thermal spike model [7]. Unlike implantation in ZrN, irradiation did not result in the combination of the 2A modes indicating less stoichiometric defects retained after irradiation. The TO peak also shifted from 457 to 480 cm^{-1} indicating structural strain after irradiation, Table 7.1.

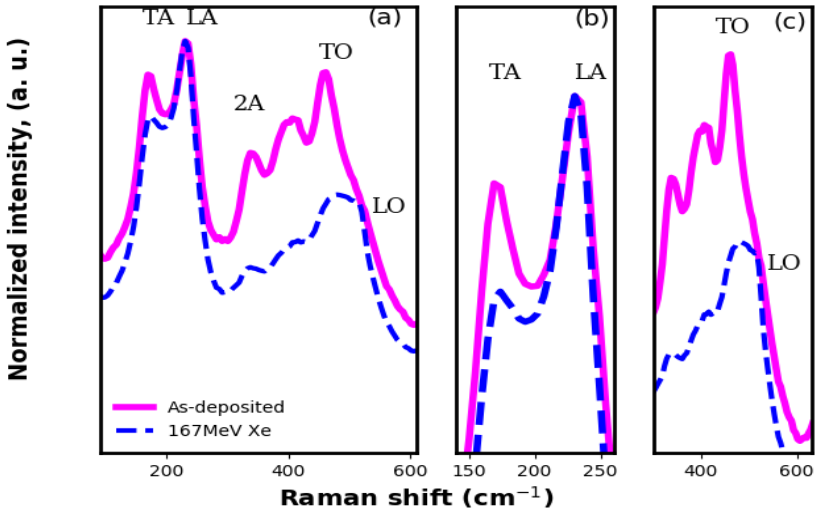

Figure 7.7: *Raman spectra of ZrN as-irradiated with Xe ions with the as-deposited spectrum to compare. (b) TA and LA modes and (c) TO and LO mode of the spectra in (a)*

Figure 7.8 is comparing the spectrum of the Xe irradiated ZrN with that of Xe implanted ZrN. The Xe irradiated ZrN spectrum resulted in a lower intensity of the TA mode compared to the Xe implanted ZrN spectrum while the LA mode remained the same. This points to the annealing effects of SHI irradiation. The 2A modes are still visible in the SHI irradiated ZrN spectrum while they are combined in the Xe implanted ZrN spectrum. This indicates fewer stoichiometric defects retained in the SHI irradiated ZrN compared to the implanted ZrN. The intensity of the TO peaks are comparably the same in both SHI irradiated and implanted ZrN implying similar amount of N defects retained after both treatments.

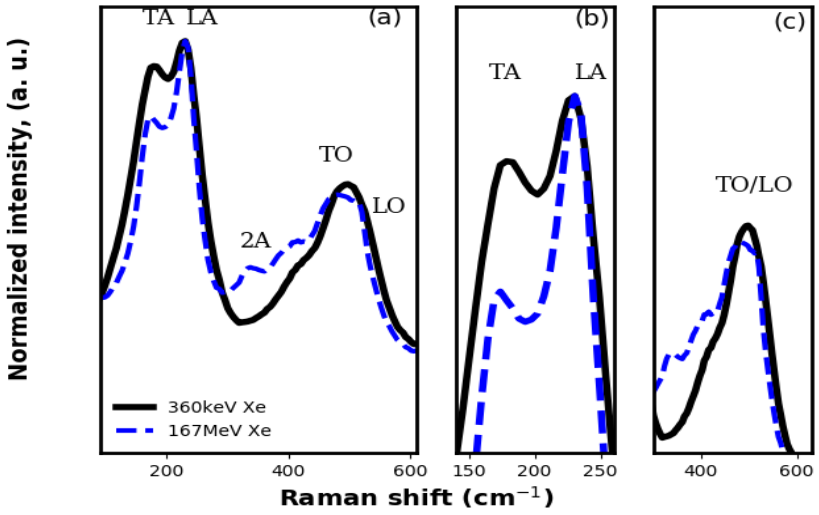

Figure 7.8: *Raman spectra of ZrN as-irradiated with Xe ions with the Xe as-implanted spectrum. (b) TA and LA modes and (c) TO and LO modes of the spectra in (a)*

Figure 7.9 (a, c) shows the optical microscope image of ZrN cross-section superimposed by a cluster image (distribution map). Figure 7.9(b, d) shows the average Raman spectra over different damage levels corresponding to each colour in the distribution map. The average distribution map is divided into the damage section, undamaged section and the Si substrate, corresponding to each colour in the map. SHI irradiation was found to cause average damage from the surface to about 10 μm below the surface. This average damage Raman spectrum is characterized by the combination of the 2A modes and a subsequent decrease in the intensity of both the 2A and TO modes, in figure 7.9(d). There is a maximum energy loss of 30 keV/nm on the surface and dominates up to about a depth of 7 μm below the surface. From about 7 μm to about 10 μm below the surface, maximum point defects are created as observed from the SRIM simulation. This is in agreement with the SRIM prediction that maximum atomic collisions are created at a projected range of about 9 μm. The difference in the surface Raman spectrum and average cross-sectional Raman spectrum might be due to the combination of defects retained by both nuclear and electronic energy loss in the latter.

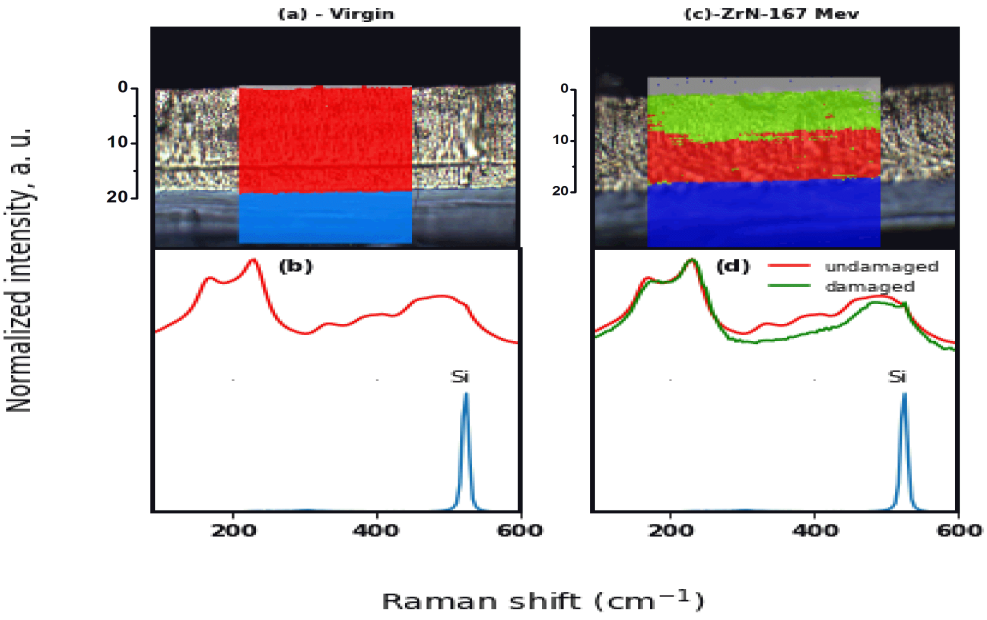

Figure 7.9: *(a, c) Cross-sectional optical microscope image with superimposed cluster distribution maps of as-deposited and Xe irradiated at 167 MeV. (b, d) Average Raman spectra of different levels of damage*

7.3 Thermal Annealing

Thermal annealing was performed on the ZrN samples implanted with Eu and Xe ions of energy 360 keV at 800 and 900 ^{o}C for 5h. The change in the structures was characterized by Raman spectroscopy. Figure 7.10 (a) shows the Raman spectra of annealed Eu implanted ZrN and Eu-implanted ZrN. Thermal annealing at 800 ^{o}C resulted in the appearance of 2A and LO modes accompanied by the increase in intensity of TO mode indicating the annealing of some stoichiometric defects. This is due to the recombination of N atoms with their vacancies and therefore, decrease in stoichiometric defects. There is also a broadening of the LA mode which could indicate annealing out of structural defects and leading to recovery of the original structure. Peak shifts were also observed with the TA shifting from 174 to 170 cm^{-1} and LA from 226 to 222 cm^{-1} compared to the Eu implanted ZrN. These indicated a reduction in structural strain in the annealed samples. Annealing at 900 ^{o}C resulted in further increase in

intensity of the 2A, TO and LO peaks. These indicate the recombination of N atoms with their vacancies and therefore, a decrease in stoichiometric defects. However, the increase in the TO, LO and only the TA mode might indicate a formation of N_{Zr} antisite defects, where N atoms recombine with Zr vacancies. Similar defects were reported in the transition metal nitride, HfN [10], where N vacancies were varied and the formation of N_{Hf} antisites were reported. Further peak shifts were observed, with TA from 170 to 165 cm^{-1} and the LA from 222 to 208 cm^{-1} compared to the 800 ^{o}C spectrum. This is an indication of a further reduction in structural strain.

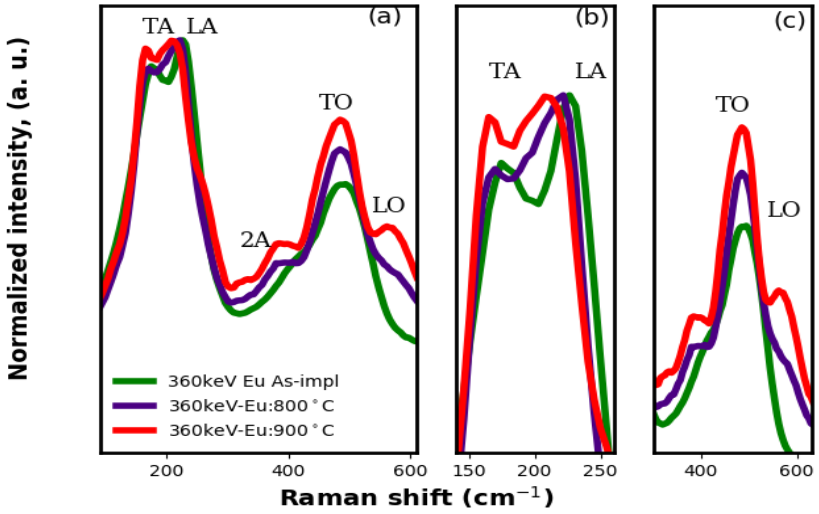

Figure 7.10: *Raman spectra of ZrN as-implanted (as-imp) sample with Eu ions and then annealed at 800 and 900 ^{o}C. (b) TA and LA modes and (c) TO and LO modes of the spectra in (a)*

Figure 7.11 is the Raman spectra of Xe implanted ZrN and implanted and then annealed ZrN at 800 and 900 ^{o}C for 5h. An increase in the intensity of TA mode while the intensity of LA mode remains the same was observed in the samples annealed at 800 ^{o}C and this was followed by the appearance of both the 2A modes. The intensity of the TO mode also increased and the LO mode was pronounced. These results indicate N atoms recombining with their vacancies followed by a decrease in stoichiometric defects and creation of N_{Zr} antisite defects as was explained above. Peak shifts were also observed with TA from 178 to 166 cm^{-1}, LA from 230 to 223 cm^{-1} compared to the as-implanted ZrN, indicating a reduction in structural strain. Thermal annealing at 900 ^{o}C results in a similar structure as the 800 ^{o}C annealed sample with a slight increase in the intensity of the TO mode and an increase in the intensity of the

LO mode. There is however, a further shift of the LA mode to 213 cm^{-1} while TA remains the same, indicating further reduction in strain. Comparing the annealed spectrum of Eu at 800 ^{o}C and 900 ^{o}C with that of Xe, it can be seen that it is easier to anneal out the damage at these temperatures for Xe implanted ZrN than it is for Eu implanted ZrN. More strain is reduced in Xe implanted ZrN than in Eu implanted ZrN. This might be due to the mass difference between Xe and Eu, where the slightly heavier Eu will occupy slightly more space in the structure than Xe.

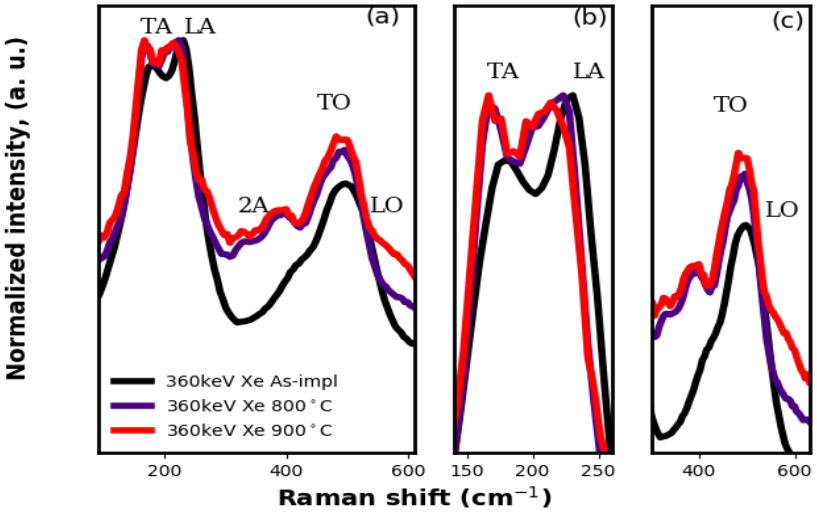

Figure 7.11: *Raman spectra of ZrN as-implanted (as-impl) with Xe ions and then annealed at 800 and 900 ^{o}C for 5h. (b) TA and LA modes and (c) TO and LO mode of the spectra in (a)*

Thermal annealing was also performed on the SHI irradiated ZrN at 800 and 900 ^{o}C for 5h. Figure 7.12 shows the Raman spectra of the irradiated ZrN and the irradiated then annealed ZrN. Thermal annealing at 800 ^{o}C resulted in the increase in the intensity of the TA mode and an appearance of a peak between the TA and LA modes at around 200 cm^{-1}. This peak resembles a peak for a cubic-Zr_3N_4 [13]. This is followed by an increase in the intensity of the 2A modes while the TO mode remains the same. These might indicate annealing of ZrN into a different structure. There is no significant peak shifts, therefore, the compressive strain together with high temperature leads to the formation of c-Zr_3N_4 phase [13].

Thermal annealing at 900 ^{o}C resulted in the decrease in the intensity of the LA mode while TA remained the same compared to the irradiated sample and there is an increase in the intensity

of the peak around 200 cm^{-1}. These are accompanied by an increase in the intensity of the 2A, TO modes and the appearance of the LO mode. The decrease in the LA intensity and increase in the TO intensity indicates N_{Zr} antisite defects in the new structure [10].

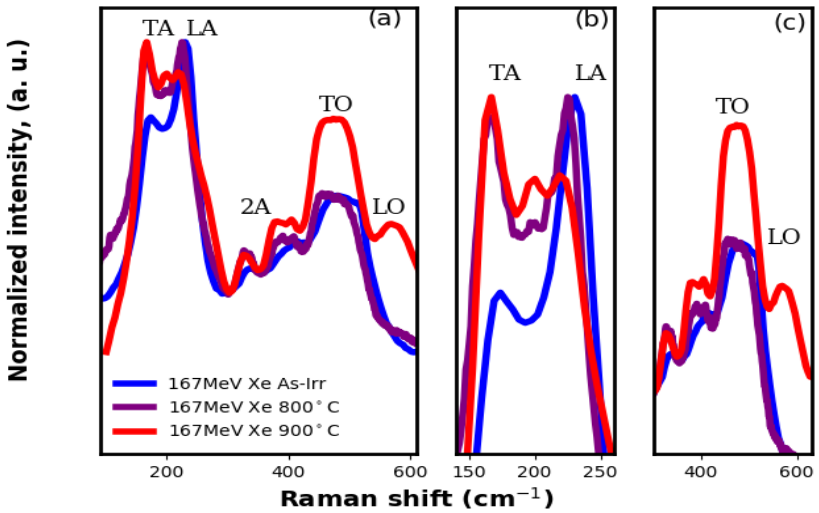

Figure 7.12: *Raman spectra of ZrN as-irradiated (as-irr) with Xe ions and then annealed at 800 and 900 °C for 5h. (b) TA and LA modes and (c) TO and LO modes of the spectra in (a)*

Table 7.1 is the summary of the TA, LA, TO, LO and 2A modes due to deposition, implantation, irradiation and thermal annealing compared with Raman peaks from literature. From the table it can be seen that the optic region shifts to higher frequencies due to implantation and irradiation indicating strain induced in the structure. Annealing of the irradiated ZrN resulted in the appearance of a peak between TA and LA due to the formation of c-Zr_3N_4. Thermal annealing caused the peak shifts to lower frequency indicating annealing of damages. In summary annealing of highly defective ZrN (Eu and Xe implanted structures) resulted in the similar structures, while that of less defective ZrN (Xe irradiated structure) resulted in a different structure with N concentration close to the as-deposited ZrN.

Table 7.1: Summary of the peak positions of the as-deposited, as-impl (as-implanted) Eu and Xe, as-irr (as-irradiated) Xe and all their annealed spectra at 800 and 900 ^oC

Modes (cm^{-1})	**TA, LA**	**2A**	**TO, LO**
Literature[2, 6, 15]	150-173,200-260	325-355, 400-525	460-580
As-deposited	169, 230	338, 407	457, 510
As-imp (360keV, Eu)	174.7, 226.5	416.7	494
Annealed 800^{o}C, Eu	170, 222	380	485, 567
Annealed 900^{o}C, Eu	165, 208	334, 385	485, 562
As-impl (360keV, Xe)	178.8, 230.5	416	498
Annealed 800^{o}C, Xe	166.7, 223	330.5, 395	495.7
Annealed 900^{o}C, Xe	166.7, 213.8	325.8, 399.7	495.7, 586
As-irr (167MeV, Xe)	174, 231	333, 416	480
Annealed 800^{o}C, Xe	168, 225	327, 391	456
Annealed 900^{o}C, Xe	167, 219	327, 382	474, 569

7.4 Migration behaviour of Eu

The migration behaviour of implanted Eu in ZrN was investigated by RBS after annealing at 800 and 900 ^{o}C for 5h. The maximum energy of the RBS system used was not enough to completely resolve Eu from ZrN. To get the Eu peak in figure 7.13, the as-deposited ZrN and Eu implanted ZrN spectra were normalized and then subtracted from each other to get the Eu distribution which was then fitted using a Gaussian function. The RBS energy-channels were converted to depth using energy loss factor and ZrN atomic density of 8.2638×10^{22} atoms/cm^3.

The fitted distribution together with the experimental distribution are compared to the SRIM simulation. The SRIM simulation resulted in a higher full-width-half-maximum (FWHM) than the experimental distribution. Both distributions, however, resulted in similar projected range of about 60 nm. The clear distinction in FWHM between the two distributions can be explained to be due to the fact that SRIM does not take into account the structural changes and reorganization that happen during to implantation [16].

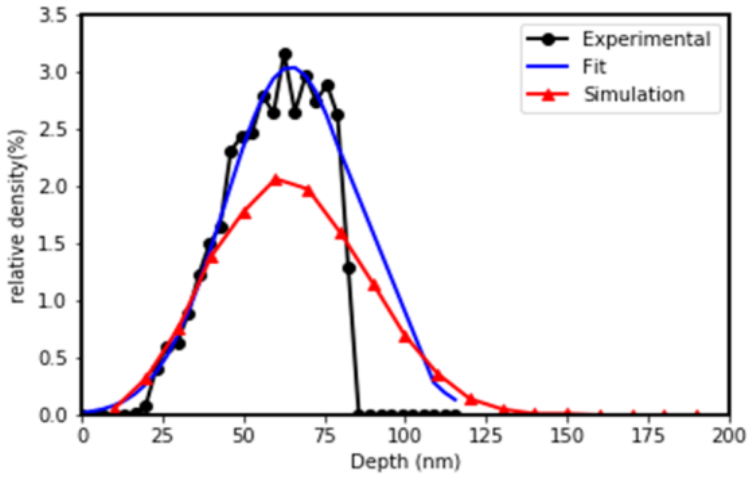

Figure 7.13: *Europium depth profile in ZrN at room temperature determined by RBS with a fitted distribution shown and compared to the SRIM-2012 distribution.*

The depth profiles of Eu implanted ZrN and Eu implanted after annealing at 800 and 900 ^{o}C for 5 hours are shown in figure 7.14. The Eu depth profiles of the 800 and 900 ^{o}C annealed samples show no significant change indicating no migration of Eu in ZrN. These results suggest

that ZrN could be an effective diffusion barrier of Eu at high operational temperatures of a nuclear reactor. Though the results are promising for the use of ZrN as a possible diffusion barrier in fast-neutron reactors, the retainment of Eu in ZrN needs to be investigated further under similar conditions as those in the nuclear reactor to validate the applicability of ZrN in nuclear environment.

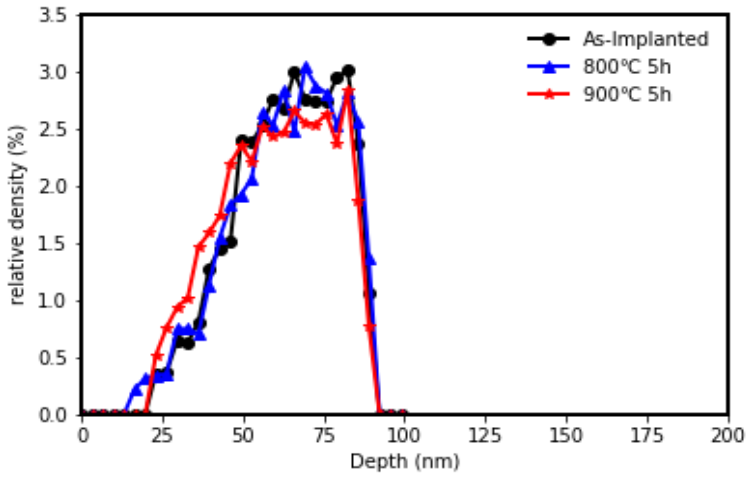

Figure 7.14: *Eu depth profiles (from RBS) of Eu implanted ZrN at RT and after annealing at 800 and 900 °C for 5 hours*

Bibliography

[1] Chen, C.C., Liang, N.T., Tse, W.S., Chen, I.Y. and Duh, J.G., (1994). 'Raman spectra of titanium nitride thin films'. *Chinese journal of physics*, 32(2), pp.205-210.

[2] Spengler, W. and Kaiser, R., (1976). 'First and second order Raman scattering in transition metal compounds'. *Solid State Communications*, 18(7), pp.881-884.

[3] Spengler, W., Kaiser, R., Christensen, A.N. and Müller-Vogt, G., (1978). 'Raman scattering, superconductivity, and phonon density of states of stoichiometric and nonstoichiometric TiN'. *physical review b*, 17(3), p.1095.

[4] Spengler, W., Kaiser, R. and Bilz, H., (1975). 'Resonant Raman scattering in a superconducting transition metal compound- TiN'. *Solid State Communications*, 17(1), pp.19-22.

[5] Montgomery Jr, G.P., Klein, M.V., Ganguly, B.N. and Wood, R.F., (1972). 'Raman scattering and far-infrared absorption induced by silver ions in sodium chloride'. *Physical Review B*, 6(10), p.4047.

[6] Constable, C.P., Yarwood, J. and Münz, W.D., (1999). 'Raman microscopic studies of PVD hard coatings'. *Surface and Coatings Technology*, 116, pp.155-159.

[7] Kuznetsov, K.B., Kovalev, I.A., Nechaev, A.N., Ogarkov, A.I., Shevtsov, S.V., Chernyavskii, A.S. and Solntsev, K.A., (2016). 'Stability of the structure of compact zirconium nitride ceramics to irradiation with high-energy xenon ions'. *Inorganic Materials*, 52(12), pp.1235-1239.

[8] Klein, M.V., Holy, J.A. and Williams, W.S., (1978). 'Raman scattering induced by carbon vacancies in Ti C x'. *Physical Review B*, 17(4), p.1546.

[9] Belyansky, M., (2012). 'Thin-Film Strain Engineering and Pattern Effects in Dielectrics CVD'. *Handbook of Thin Film Deposition*, 89.

[10] Stoehr, M., Seo, H.S., Petrov, I. and Greene, J.E., (2008). 'Effect of off stoichiometry on Raman scattering from epitaxial and polycrystalline HfN x (0.85≤ x≤ 1.50) grown on MgO (001)'. *Journal of Applied Physics*, 104(3), p.033507.

[11] Benyagoub, A., Audren, A., Thome, L. and Garrido, F., (2006). 'Athermal crystallization induced by electronic excitations in ion-irradiated silicon carbide'. *Applied physics letters*, 89(24), p.241914.

[12] Audren, A., Monnet, I., Gosset, D., Leconte, Y., Portier, X., Thome, L., Garrido, F., Benyagoub, A., Levalois, M., Herlin-Boime, N. and Reynaud, C., (2009). 'Effects of electronic and nuclear interactions in SiC'. *Nuclear Instruments and Methods in Physics Research Section B: Beam Interactions with Materials and Atoms*, 267(6), pp.976-979.

[13] Chhowalla, M. and Unalan, H.E., (2005). 'Thin films of hard cubic Zr_3N_4 stabilized by stress'. *Nature materials*, 4(4), p.317.

[14] Ren, J., Ward, M., Kinnell, P., Craddock, R. and Wei, X., (2016). 'Plastic deformation of micromachined silicon diaphragms with a sealed cavity at high temperatures'. *Sensors*, 16(2), p.204.

[15] Cassinese, A., Iavarone, M., Vaglio, R., Grimsditch, M. and Uran, S., (2000). 'Transport properties of ZrN superconducting films'. *Physical Review B*, 62(21), p.13915.

[16] Ziegler, J.F. and Biersack, J.P., (1985). 'The stopping and range of ions in matter'. *In Treatise on heavy-ion science* (pp. 93-129). Springer, Boston, MA.

Chapter 8

Summary and future work

The effects of Eu and Xe implantation and Xe SHI irradiation of the nanocrystalline ZrN films were investigated. ZrN layers of 20 μm thickness were successfully deposited onto silicon substrate. The as-deposited ZrN was investigated using cross-sectional SEM, GIXRD and Raman spectroscopy, while the Eu and Xe implanted ZrN and Xe irradiated ZrN were investigated using Raman spectroscopy. The migration behaviour of implanted Eu was investigated using RBS after annealing at 800 and 900 ^{o}C for 5 hours. GIXRD results confirmed that an fcc structure with an Fm$\overline{3}$m space group was deposited with the (311) plane most preferred. The as-deposited ZrN layers revealed bands in the Raman spectrum of first-order Raman scattering due to the perturbed octahedral symmetry by sample preparation induced defects. The following modes were reported as confirmed by literature, the transverse and longitudinal acoustic modes, TA and LA, respectively, transverse and longitudinal optical modes, TO and LO, respectively, and the low-frequency second-order acoustic Raman scattering, 2TA and TA+LA labeled 2A.

Large amounts of radiation damage were retained in the Eu and Xe implanted ZrN layers. These layers resulted in the increase in the intensity of the TA mode, broadening of both the TA and LA modes, the combination of the 2A modes and a significant decrease in the intensity of the TO mode. These resulted in ZrN implanted structures with high stoichiometric defects and high N vacancies. Both Eu and Xe implantation resulted in similar defects with Eu creating slightly more strain due to its heavier mass compared to Xe. The Xe irradiated ZrN resulted in less structural strain compared to the Xe implanted ZrN with maximum damage of

2.5 dpa at $\sim$ 10 μm below surface and maximum electronic energy loss of 30 keV/nm on the surface. Raman spectra of the irradiated layers exhibited all bands with a decrease in the TA intensity characterizing the annealing effects of SHI irradiation.

Thermal annealing of both Eu and Xe implanted ZrN samples at 800 and 900^{o}C for 5h resulted in the reappearance of the LO peaks and the increase in the intensity of the TO peaks. This was explained to be due to recombination of N atoms with their sites and a subsequent formation of N_{Zr} antisite defects. Annealing of the Xe irradiated ZrN resulted in appearance of a peak between the TA and LA modes. Implantation, irradiation and thermal annealing in the main resulted in ZrN structures with less N concentration compared to the as-deposited ZrN. However, annealing at 900^{o}C of both the implanted and irradiated ZrN samples resulted in the N concentrations closer to the as-deposited ZrN. The migration behaviour of Eu in ZrN was also investigated and no migration was observed after annealing at both 800 and 900^{o}C for 5h. These results are promising but further investigation under nuclear environment conditions need to be conducted to make the results relevant.

There is an opportunity to further study and confirm the formation of the c-Zr_3N_4 phase in the SHI irradiated ZrN after annealing using different experimental techniques such as XRD and TEM. The effect of irradiation on the change in stoichiometry of ZrN_x needs to be quantified using high energy RBS. Using a high energy RBS to improve mass resolution, the migration behavior of Eu will be studied further. The effect of irradiation in the migration of Eu in ZrN will also be investigated. Similar studies will also be conducted on Xe irradiation in ZrN, this will be achieved by using high energy RBS.

Appendix

This work was presented at the 2018 conference of the South African Institute of Physics (SAIP). It has also culminated in a publication in the September 2019 issue of the Nuclear Instruments and Methods in Physics Research B, volume 461, as an article titled: 'Slow and swift heavy ions irradiation of zirconium nitride (ZrN) and the migration behaviour of implanted Eu'.